The Microphysics of Stratiform Precipitation During OLYMPEX: Compatibility Between Triple-Frequency Radar and Airborne In Situ Observations

(Article begins on next page)

02 May 2024

The Microphysics of Stratiform Precipitation During OLYMPEX: Compatibility Between Triple-Frequency Radar and Airborne In Situ Observations

Frédéric Tridon[1,2], Alessandro Battaglia[1,3], Randy J. Chase[4], F. Joseph Turk[5], Jussi Leinonen[5,6], Stefan Kneifel[2], Kamil Mroz[3], Joseph Finlon[4], Aaron Bansemer[7], Simone Tanelli[5], Andrew J. Heymsfield[7], and Stephen W. Nesbitt[4]

[1]Earth Observation Sciences, Department of Physics and Astronomy, University of Leicester, Leicester, UK, [2]Institute for Geophysics and Meteorology, University of Cologne, Cologne, Germany, [3]National Center for Earth Observation, University of Leicester, Leicester, UK, [4]Department of Atmospheric Sciences, University of Illinois at Urbana-Champaign, Urbana, IL, USA, [5]Jet Propulsion Laboratory, California Institute of Technology, Pasadena, CA, USA, [6]Environmental Remote Sensing Laboratory, École Polytechnique Fédérale de Lausanne, Lausanne, Switzerland, [7]National Center for Atmospheric Research, Boulder, CO, USA

Abstract The link between stratiform precipitation microphysics and multifrequency radar observables is thoroughly investigated by exploiting simultaneous airborne radar and in situ observations collected from two aircraft during the OLYMPEX/RADEX (Olympic Mountain Experiment/Radar Definition Experiment 2015) field campaign. Above the melting level, in situ images and triple-frequency radar signatures both indicate the presence of moderately rimed aggregates. Various mass-size relationships of ice particles and snow scattering databases are used to compute the radar reflectivity from the in situ particle size distribution. At Ku and Ka band, the best agreement with radar observations is found when using the self-similar Rayleigh-Gans approximation for moderately rimed aggregates. At W band, a direct comparison is challenging because of the non-Rayleigh effects and of the probable attenuation due to ice aggregates and supercooled liquid water between the two aircraft. A variational method enables the retrieval of the full precipitation profile above and below the melting layer, by combining the observations from the three radars. Even with three radar frequencies, the retrieval of rain properties is challenging over land, where the integrated attenuation is not available. Otherwise, retrieved mean volume diameters and water contents of both solid and liquid precipitation are in agreement with in situ observations and indicate local changes of the degree of riming of ice aggregates, on the scale of 5 km. Finally, retrieval results are analyzed to explore the validity of using continuity constraints on the water mass flux and diameter within the melting layer in order to improve retrievals of ice properties.

1. Introduction

Diabatic processes, and particularly condensational heating, play an essential role on the dynamics of mid-latitude precipitation systems (Crezee et al., 2017; Papritz & Spengler, 2015). While it is generally agreed that they deepen cyclones and strengthen wind and precipitation associated with storms (Coronel et al., 2015; de Vries et al., 2010; Grams et al., 2011; Willison et al., 2013), the magnitude of this intensification is case to case dependent and still debated. The latent heat exchanged during the formation of precipitation involves a variety of microphysical processes whose parameterizations in numerical models are still imperfect (Chagnon et al., 2013; Dearden et al., 2014). Therefore, accurate characterization of ice and rain microphysics profiles is crucial to help advance our understanding of midlatitude precipitation systems.

The vertical structure of latent heating within mesoscale convective systems (MCS) is known to differ strongly between convective and stratiform regions (e.g., Houze, 1982; 1989). In order to properly represent the effect of latent heating on the large-scale environment, the contribution of stratiform regions to the net latent heat profile must not be neglected (Hartmann et al., 1984). Furthermore, studies that have investigatedz the influence of vertical structure of latent heating assume geographically uniform vertical heating profiles (Schumacher et al., 2004), while it is important to take into account the variability of the magnitude

Project Administration: Alessandro Battaglia

Resources: Jussi Leinonen, Stefan Kneifel, Joseph Finlon, Aaron Bansemer, Simone Tanelli, Andrew J. Heymsfield

Supervision: Alessandro Battaglia

Writing - review & editing: Frédéric Tridon, Alessandro Battaglia, Randy J. Chase, Jussi Leinonen, Kamil Mroz, Simone Tanelli, Andrew J. Heymsfield, Stephen W. Nesbitt

and shape of these profiles both at the global scale (Liu et al., 2015; Schumacher et al., 2004) and at the storm scale (Marinescu et al., 2016).

Such variability is enhanced in extratropical cyclones where the high horizontal gradient of temperature within frontal systems complexifies both the effect of moist processes on storm dynamics (Coronel et al., 2015; Dearden et al., 2014; Joos & Wernli, 2012) and the retrieval of latent heat itself (Tao et al., 2019). Therefore, more observations of the full microphysics profiles in midlatitude precipitating systems are needed at high resolution in order to evaluate and improve the representation of microphysics in models.

Radars with frequency in the range between 9 and 95 GHz have demonstrated great effectiveness in vertically resolving cloud precipitation processes. By exploiting the frequency dependence of the interaction between hydrometeors and microwave radiation (Lhermitte, 1990), multifrequency radars have the potential to provide improved profiles of precipitation rates and of the microphysical properties of the ice and rain particle size distributions (PSDs). Previously, several multifrequency cloud radar techniques have been proposed to derive precipitating ice (Leinonen et al., 2018; Mason et al., 2018; Matrosov, 1998; Turk et al., 2011) and rain (Firda et al., 1999; Mason et al., 2017; Tridon et al., 2017) in stratiform systems, but few of them provide a simultaneous description of the ice and rain profile (Gaussiat et al., 2003; Grecu et al., 2011; 2016; Seto et al., 2013). Three points make such a retrieval challenging:

- The properties of ice crystals are extremely variable (size, shape, and structure), which makes their microwave scattering properties complex. Not only does deposition lead to various shapes but also ice particle growth by aggregation and riming complicate their structure and bulk density. While the degree of riming can fundamentally change the density of ice aggregates, until recently, most of the ice retrievals have assumed a constant ice density or a single mass-size relation (Gaussiat et al., 2003; Grecu et al., 2011; 2016; Seto et al., 2013; Turk et al., 2011).
- Within the transition from ice to rain, the melting layer produces significant attenuation (Matrosov, 2008), which is challenging to estimate because the scattering properties of melting ice crystals are poorly characterized.
- In rain, both scattering and attenuation significantly affect the differences in the reflectivity observed at different radar frequencies and additional information (such as Doppler velocity, Doppler spectra, or path-integrated attenuation, PIA) is generally necessary to disentangle these two effects, a critical aspect for reducing potential ambiguities in the retrieval.

This study proposes a methodology for retrieving full profiles of ice and liquid stratiform precipitation by combining the airborne multifrequency radar and radiometer observations collected on 1 December 2015 during the Global Precipitation Measurement (GPM) ground validation Olympic Mountain Experiment (OLYMPEX) and its radar component Radar Definition Experiment 2015 (RADEX'15), which took place over the Olympic Peninsula (Washington State, USA) in late 2015 (Houze et al., 2017). Since numerous studies have recently shown that rimed and unrimed ice particles present contrasting signatures in triple-frequency measurements (Chase et al., 2018; Kneifel et al., 2015; Stein et al., 2015; Yin et al., 2017), particular attention is made on the ice retrieval with the use of various state-of-the-art scattering models corresponding to different degrees of riming. The retrieval is tested for an aircraft transect where colocated airborne in situ observations of both ice and rain particles allow direct comparisons with the retrieval.

The paper is structured as follows: The case study and flight transect under focus are described in section 2, as well as the corresponding radar and in situ measurements. Section 3 summarizes the various ice scattering models, which are then used for computing radar reflectivities from in situ PSD and presents direct comparisons with radar observations. Section 4 details the retrieval algorithm, which is then applied to the remote sensing observations in section 5. Concluding remarks are presented in section 6.

2. Case Study

On the 1 December 2015, a weakening 500-hPa trough and strong moist southwesterly flow lead to widespread stratiform precipitation over the Olympic Peninsula (Houze et al., 2017). The thermodynamic profile of the atmosphere (Figure 1) corresponds to a typical frontal structure with warm-air advection below a stable layer and saturated conditions (Petersen & Houze, 2017).

During several hours, the National Aeronautics and Space Administration (NASA) DC-8 aircraft equipped with the Airborne Precipitation Radar Third Generation (APR-3 radar,Durden & Tanelli, 2017;
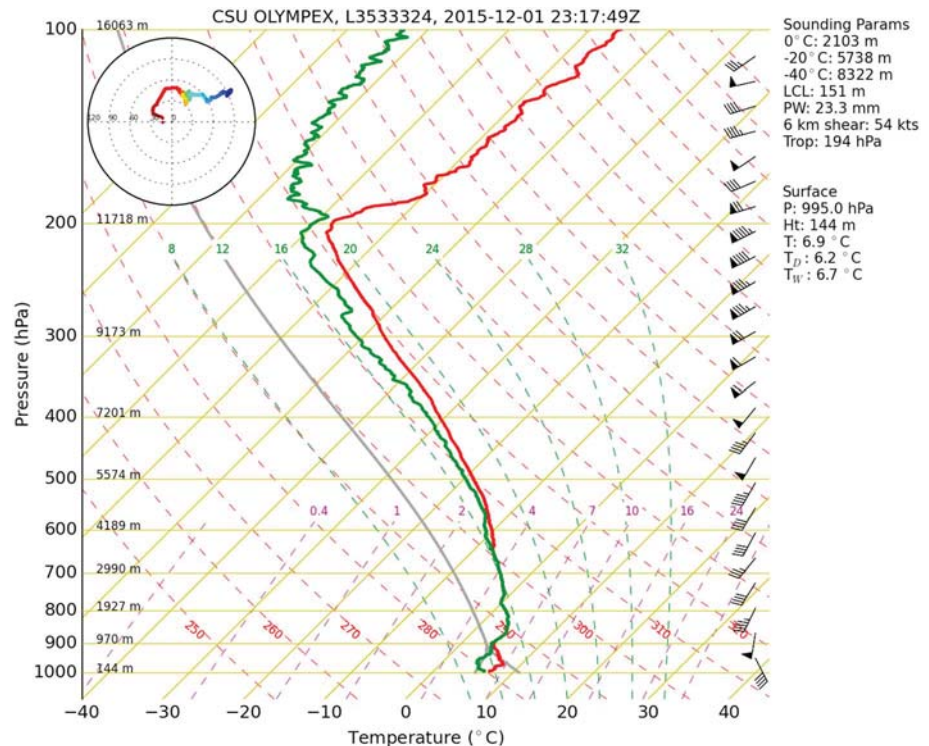
Figure 1. Skew-T log-P diagram of the atmospheric temperature (continuous red line) and dew-point temperature (continuous green line) profiles from the Rawinsonde sounding launched at NPOL site on 1 December 2015, at 2317 UTC (extracted from http://olympex.atmos.washington.edu/archive/reports/20151201-2/soundings/research.skewt. 201512012300.csu.png). NPOL = NASA S Band Dual-Polarimetric Radar; OLYMPEX = Olympic Mountain Experiment.

Sadowy et al., 2003) flew over this precipitation system as it crossed over the mountains in southwest-northwest tracks over the location of the ground-based NASA S Band Dual-Polarimetric Radar (NPOL). In particular, the leg starting at 2308 UTC (Figure 2) was coordinated with the University of North Dakota (UND) Citation aircraft which collected in situ observations of ice particles at 3 km above sea level (−4.5 °C) before descending over the ocean through the melting and rain layers.

Direct comparisons between airborne remote sensing and in situ observations are possible only if they are very well matched in both space and time. This is very challenging to achieve because the two aircraft fly at different velocities. With both aircraft flying from the mountain range toward the sea, this is one of the few coordinated legs of the campaign for which the two aircraft were flying toward the same direction. It maximizes the matching between observations, with simultaneous observations at 2320 UTC in the vicinity of the NPOL radar (whose position is indicated by the black disk in Figure 2) and largest time mismatch of about 5 min over the Olympic mountains. Not only the microphysical properties can change in the 5-min difference of the observations made by the two aircraft, but also, the particularly intense winds observed during this precipitation system (20 m/s at 3-km height) can lead to a significant 6-km displacement of the volume sampled between both observations. Since they were flying in a direction almost directly opposite to the air flow, a simple linear correction of the Citation position similar to the one proposed by Hogan et al. (2006) will be used in sections 3.2 and 5.3 in order to optimize the matching between observations, with the assumption that there is no significant temporal evolution of the observed system between both observations.

2.1. Remote Sensing Observations
Data from the three radars were collected and merged into common field of view (FOV). As the DC-8 flew in straight-line segments up and down the Olympic Peninsula and out over the Pacific Ocean, each nearest-to-nadir APR-3 beam was identified. This may not always be the middle beam (APR-3 collects data at 24 positions across scan) owing to slight variations in the aircraft attitude and rolling angle. With knowl-
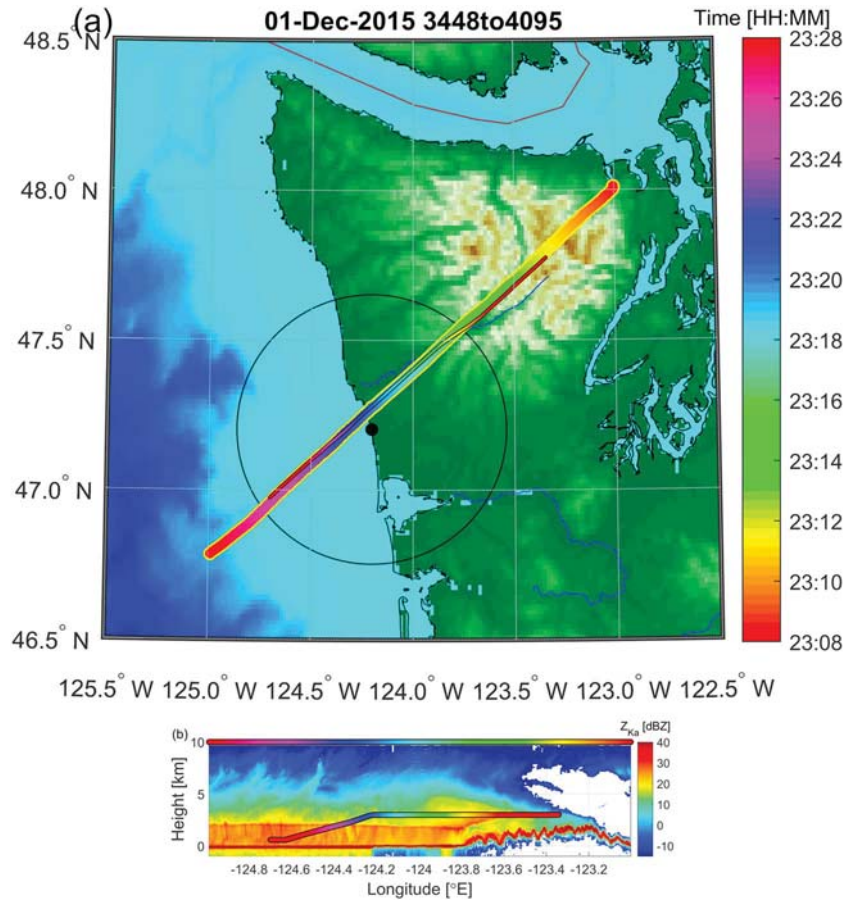
Figure 2. (a) Time (for time-color mapping see the colorbar) of DC-8 (thick line) and Citation (thin line) aircraft paths as they flew across the Olympic Peninsula from the Olympic Mountains range toward and beyond the NPOL radar (black dot) on the Pacific Coastline. (b) Altitude of the Citation aircraft within the curtain of Ka band reflectivity observed by DC-8 with its corresponding acquisition time modulated by the same color mapping used in panel (a). Similarly for comparison, the acquisition time of DC-8 observations is plotted at an arbitrary 10-km altitude. The best matching in time is obtained around 2320 UTC as indicated by the arrow in panel (b). NPOL = NASA S Band Dual-Polarimetric Radar.

edge of the height from each APR-3 surface bin, the observations of each APR-3 radar were binned into common 30-m profiles.

From APR-3 observations, three reflectivity profiles are obtained at Ku (13.4 GHz), Ka (35.6 GHz), and W band (94.9 GHz). Calibration is made using clear air observations of the ocean surface backscatter cross section (Tanelli et al., 2006). At a given wavelength λ and for a particle size distribution $N(D)$, the radar reflectivity Z_e is defined using a reference dielectric factor for liquid water at centimeter wavelength (0.93):

$$Z_e \equiv \frac{\lambda^4}{0.93\,\pi^5} \int_0^{D_{\max}} N(D)\sigma_b(D)\mathrm{d}D, \tag{1}$$

where $\sigma_b(D)$ is the radar backscattering cross section of a particle of maximum dimension D. With this convention, a millimeter wavelength radar measures the same reflectivity as a centimeter wavelength radar for a Rayleigh scattering ice cloud, which facilitates their comparison. On the other hand, observed reflectivity of liquid Rayleigh targets at 0 °C are larger at Ku than at Ka and W by 0.2 dB and 1.2 dB, respectively (Lhermitte, 1990). Thanks to absorption models (Liebe, 1989; Rosenkranz, 1993; 1998), radar attenuation due to atmospheric gases is computed from the closest sounding (Figure 1). Having been sent 5 min before the aircraft overpasses, it is well representative of the thermodynamic profile of the atmosphere for the portion of the flights to the west of the Olympic mountain range.
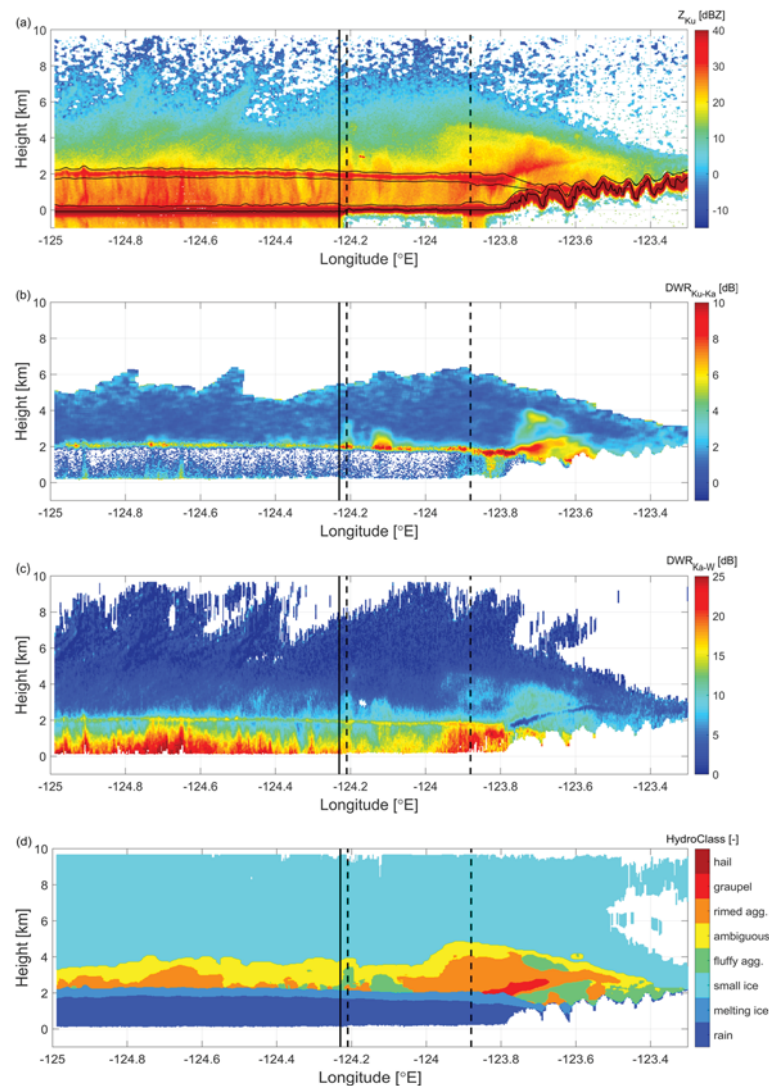
Figure 3. Time-height plots of the (a) reflectivity measured by the Ku band radar and of the ratio between (b) Ku and Ka reflectivity and (c) between Ka and W band reflectivity, and of (d) a coarse classification of hydrometeor types on 1 December 2015, for the DC-8 leg starting at 2308 UTC. In each panel, the continuous black line separates the observations made over land (to the east) and over ocean (to the west), and the dashed black lines shows the position of profiles which will be presented in Figures 10 and 11.

The strong surface return in the Ku-reflectivity (Figure 3a) clearly highlights the transition from the ocean (longitudes west of −124.2 °E) to the Quinault River valley, and finally to the Olympic mountain range. Above the surface, low reflecting ice is clearly separated from high rain reflectivity by the melting layer straddling around 2 km. An orographic enhancement is obvious with higher ice reflectivity closer to the mountains, but several short periods of enhanced reflectivity above the melting layer also suggest some local change in the ice growth microphysics processes. The pocket of high reflectivity at 3 km and −124.16°E longitude corresponds to the Citation aircraft being observed by the radar, a signature of the very good coordination between the two aircraft. Finally, nonzero reflectivities observed below the surface correspond to mirror images of the precipitation which are particularly noticeable over the Pacific Ocean (longitude lower than −124.2°E) and Quinault lake (around −123.85°E).

Multifrequency radar observations are exploited in the characterization of both ice and liquid precipitation (Battaglia, Mroz, Lang, et al., 2016). They rely on the wavelength dependence of scattering and absorption properties at millimeter wavelength. Rain drops are good absorbers, and the radar attenuation typically increases with frequency. Conversely, ice particles can be large enough to produce non-Rayleigh scattering,

which generally leads to a reduced reflectivity at higher radar frequencies. In practice, both effects are simultaneously present and sophisticated techniques are generally required in order to disentangle them (Tridon et al., 2013).

Differential reflectivity effects are readily visible when comparing the Ku (Figure 3a) and Ka (Figure 2b) reflectivity fields by considering the dual wavelength ratio (DWR), which is defined as the ratio between the reflectives (in linear units) observed by two radars with the convention of having the reflectivity of the higher frequency—which is typically smaller—in the denominator. The DWR_{KuKa} and DWR_{KaW} expressed in decibel and corrected for gas attenuation, are depicted in Figures 3b and 3c, respectively. While the Ku, Ka, and W reflectivities are equal (with all DWRs being equal to 0 dB) in the upper part of the ice cloud, where only small ice crystals are present (Rayleigh scattering at all radar frequencies), the reflectivity at higher frequencies becomes lower when ice particles grow in size with the corresponding DWR increasing particularly in the vicinity of the 0 °C isotherm. Below the melting layer, the DWRs increase toward the ground mainly due to the effect of rain attenuation. Based on these qualitative features, a coarse classification (Figure 3d) identifies the ice, melting, and rain regions as well as three rough categories of aggregates (fluffy, rimed, and ambiguous). See the appendix for details.

2.2. Airborne In Situ Observation

The Citation aircraft was equipped with state-of-the-art cloud microphysics instrumentation (Heymsfield et al., 2017; Poellot et al., 2017). During the below 0 °C part of the leg, particle size distributions (Figure 4b) were obtained via the combination of the Two-Dimensional Stereo Probe (2D-S, 225 μm $< D <$ 1 mm; Lawson et al., 2006) and HVPS3 (1 mm $< D <$ 3.25 cm) both equipped with antishattering tips and processed following Chase et al. (2018) using particle interarrival times to identify shattered artifacts (Jackson et al., 2014). The resulting PSDs are close to an exponential distribution (the difference between actual D_m and IWC and those obtained from exponential fits of the PSD are negligible, not shown) and feature large ice ($D >$ 4 mm) aggregates (examples of individual particle images can be found in Figures 10d and 11d) over the entirety of this leg (Figure 4a). During the above 0 °C part of the leg, drop size distributions (not shown) were measured by the High Volume Particle Spectrometer (HVPS3, 0.2 mm $< D <$ 3.25 cm) using strict rejection criteria such as a minimum area ratio of 0.5. Note that the concentration of drops smaller than 0.7 mm may be underestimated by the HVPS3, which would lead to a slight underestimation of the liquid water content and slight overestimation of the mean volume diameter.

During the below 0 °C part of the Citation leg, the Rosemount Icing DEtector (RICE) exhibits icing around the upwind side of the mountain range (in Figure 4a between −124 and −123.6 °CE and more particularly where the blue shading is shown). This suggests that updrafts associated with the mountain range lead to the formation of supercooled liquid water and that significant riming can be expected in this area. In situ ice water content (IWC) is not directly measured (the counterflow virtual impactor was not functioning properly during this field campaign) but calculated from the subtraction of the measured liquid water content (LWC) from the King hotwire probe and the measured total water content (TWC) from the Nevzorov deep cone probe (see orange line in Figure 4c). However, both probes are subject to significant uncertainties in the conditions encountered: overestimation of LWC due to the interaction of the hot wire with ice (Cober et al., 2001) and underestimation of TWC by the Nevzorov probe when PSDs contain particles with $D >$ 4 mm (Korolev et al., 2013). Otherwise, IWC can be derived from the PSD by integration of the mass of each individual particle, by assuming a power law relation $m(D) = \alpha_m D^{\beta_m}$ between mass and size. However, the mass-size relation is the primary source of uncertainty in estimates of IWC (Delanoë et al., 2014), and numerous $m(D)$ relations have been proposed in the literature. In particular, while the occurrence of riming is known to strongly modify the parameters of $m(D)$ relations, high-resolution Cloud Particle Imager (CPI) images of individual crystals and small aggregates clearly feature contrasting degree of riming for some portions of this leg (Figure 5), with rimed particles found near the mountain range, in agreement with the RICE signatures.

In order to clearly assess the effect of riming on the computation of IWC from the PSDs, and then on its retrieval from radar observations, it is important to use various mass-size relations encompassing a wide range of particles types, from unrimed/fluffy aggregates to high-density graupel. Figure 6 shows examples of prefactors α_m and exponents β_m of the mass-size relations from the literature that are used in this study. Note that they have been selected mainly because radar scattering computation methods are associated to them, and as a matter of fact, most of them (light to dark gray diamonds) have been derived from the
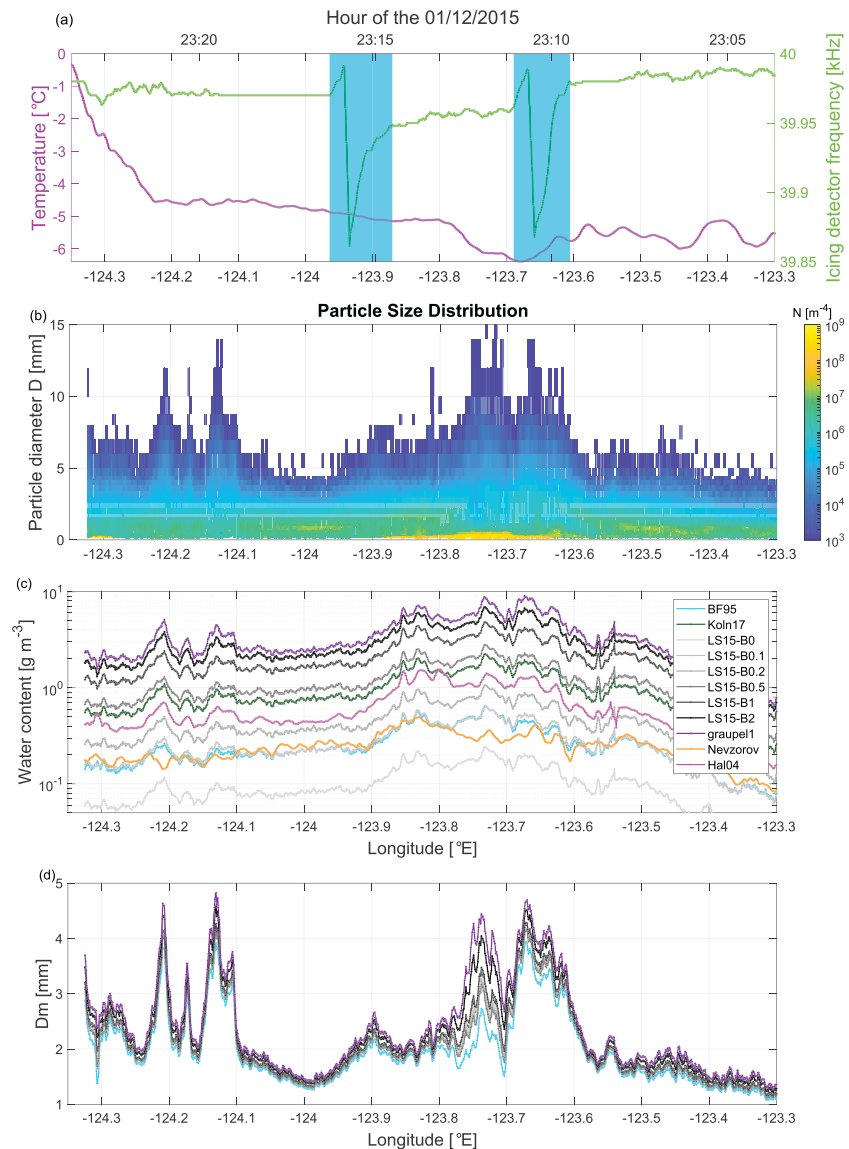
Figure 4. Different in situ measurements taken in the portion of the Citation leg above the freezing level. (a) Temperature at the Citation level with icing periods (blue shadings) highlighted by the drop of the RICE oscillation frequency with time (the oscillation frequency jumps back to the RICE nominal frequency when its heater is automatically turned on in order to remove excessive ice buildup). Corresponding (b) particle size distributions measured by the 2D-S and HVPS3, (c) IWC, and (d) D_m using various mass-size relations proposed in literature (see Figure 6). The orange and pink curves in panel (c) correspond to the Nevzorov probe measurements and AHParam estimate, respectively (see text for details). RICE = Rosemount Icing DEtector.

results of a model of aggregation and riming (Leinonen & Szyrmer, 2015) in which rimed aggregates are obtained by subsequent aggregation of ice crystals and riming in supercooled liquid clouds of increasing liquid water path from 0 to 2 kg/m² (hereafter LS15-Bxx, where the crosses refer to the liquid water path amount). This set is extended with the mass-size parameters (purple to red circles) corresponding to five empirical models of spherical graupel with increasing density. Note that only the three remaining couples of prefactors and exponents (+ markers) correspond to real observations. For a more complete review of the mass-size relations obtained from observations, please refer to Mason et al. (2018).

While the exponents of fluffy aggregates are close to $b_m = 2$ (Stein et al., 2015), the effect of riming on the mass-size relation is not well understood. In order to describe the riming process, the so-called "fill-in" model was proposed by Heymsfield (1982) and was still adopted in recent modeling studies (Brdar & Seifert, 2018; Morrison & Milbrandt, 2015). This is a two-stage process (Figure 6), where (a) the rime accumu-
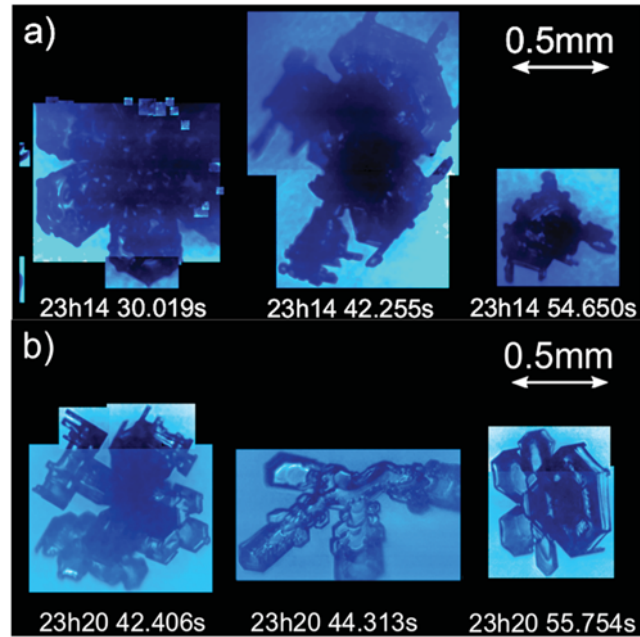
Figure 5. Examples of Cloud Particle Imager images at two locations where rimed (a) and unrimed (b) ice crystals were observed. Time stamps are indicated under each figure.

lates first in crystal interstices without changing the maximum dimension which leads to an increase of the prefactor only, and then after particles are filled in with rime, (b) the rime accretes to the outside of the particle now similar to graupel particles, leading to an increase of both prefactor and exponent, until the latter reaches the physical maximum value of β_m equals three of solid ice spheres. This assumption was corroborated by Li et al. (2018) who showed that riming starts to modify ice particle shapes when rime mass exceeds 50% of the total particle mass. Furthermore, this simplified model has been validated using observations of rimed ice crystals (Erfani & Mitchell, 2017) and allowed to link ground-based ice particle measurements with microwave radiometer observations of liquid water path (Moisseev et al., 2017).

However, there is still some debate on the validity of the fill-in model. For example, using their aggregation and riming model, Leinonen and Szyrmer (2015) showed that both parameters change when riming and aggregation happen at the same time. Using the same model but with subsequent riming and aggregation, Seifert et al. (2019) proposed a smooth parameterization which approaches asymptotically the two stages of the fill-in model. Furthermore, because their review of the mass-size relation derived from observations did not show any compelling evidence to support the two-stage model (like the few observation-derived prefactors and exponents of Figure 6 suggest), Mason et al. (2018) derived a continuous linear relation between the exponent and prefactor. Nevertheless, the exponents and prefactors corresponding to the model B crystals of Leinonen and Szyrmer (2015) seem to be in agreement with the fill-in model. This agreement motivated the derivation of the five empirical models of spherical graupel via interpolation between LS15-B2 and a solid ice sphere. The terminology of the different ice particle types is not so clear though, since the position of heavily rimed aggregates from Leinonen & Szyrmer, 2015 (2015; LS15-B1 and LS15-B2 in Figure 6) parameters in the α_m and β_m space suggests that they have already started the graupel-like growth.

During OLYMPEX, the type of precipitation was mainly stratiform and graupel formation is not expected. Therefore, among the mass-size relations shown in Figure 6, the rest of this work focuses on those corresponding to aggregates (unrimed and rimed), and a class of low-density graupel will be kept as a reference point.

When adopting the mass-size relations provided in Figure 6, the WC, the mean mass diameter D_m, the mass flux, and the mass spectrum standard deviation σ_m (see Williams et al., 2014) can be computed from the PSD $N(D)$ following
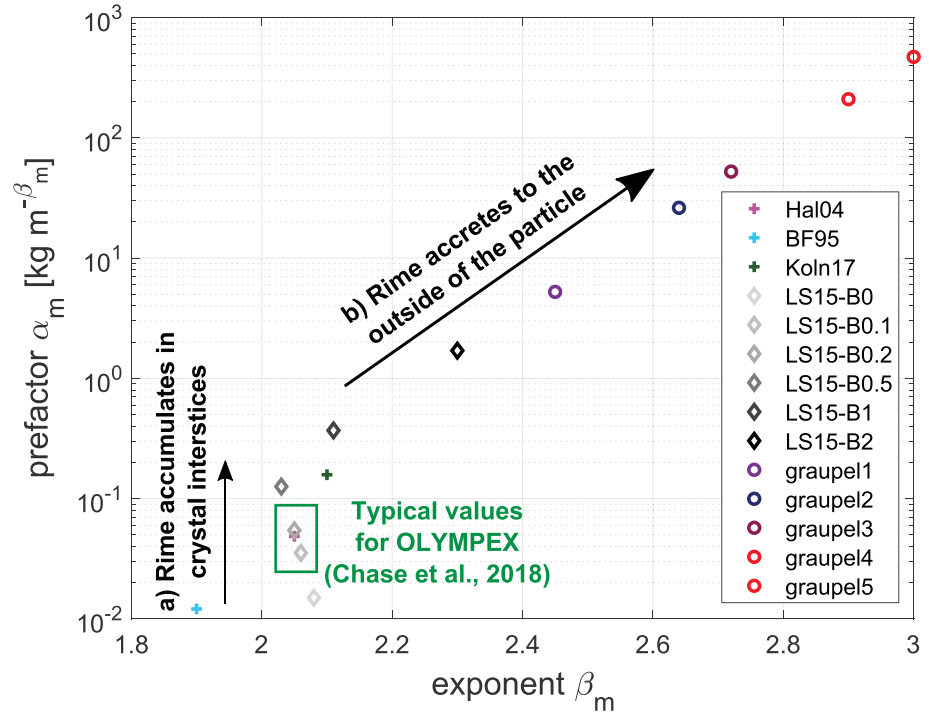
$$WC = \int_0^{D_{\max}} N(D)m(D)\mathrm{d}D, \tag{2}$$

Figure 6. Illustration of the effect of riming on the mass-size parameters prefactors α_m and exponents β_m according to the fill-in model (note that this simplified model is the subject of debate, see the text for details), and examples of parameters obtained principally from a modeling study (diamonds and circles) and from observations (+ markers). This plot is based primarily on the parameters derived by Leinonen and Szyrmer (2015) aggregation and riming model for increasingly rimed aggregates (gray diamond). For brevity and clarity, only the parameters of their model B (corresponding to riming following aggregation) are used. Also shown are parameters of particles corresponding to various degrees of riming: aggregates of unrimed bullet, columns and side-planes (hereafter BF95 ; Brown & Francis, 1995), denser aggregates of unrimed hexagonal columns (hereafter Koln17 ; Ori et al., 2014) or rimed aggregates (hereafter Heymsfield04 ; Heymsfield et al., 2004) (note that these parameters are very close to those of LS15-B0.2), as well as 5 models of spherical graupel with increasing density.

$$D_m = \frac{\int_0^{D_{\max}} N(D)m(D)D\mathrm{d}D}{WC},\tag{3}$$

$$Flux = \frac{\int_0^{D_{\max}} N(D)m(D)v_t(D)\mathrm{d}D}{WC}(p_0/p)^{0.42},\tag{4}$$

$$\sigma_m = \sqrt{\frac{\int_0^{D_{\max}} N(D)m(D)(D-D_m)^2\mathrm{d}D}{WC}},\tag{5}$$

where $v_t(D)$ is the terminal fall velocity of the ice particle of diameter D at a reference pressure p_0, computed according to Heymsfield and Westbrook (2010). The factor $(p_0/p)^{0.42}$ takes into account the increase of $v_t(D)$ with altitude (with the decrease of the pressure p).

While the mass-size relation has little influence on D_m for most of the leg (Figure 4d), it is clear that there is a large range of possible IWC from PSD observations (Figure 4c). Comparison with independent estimates of IWC can give better insight into the actual mass-size relation valid for these observations. The IWC estimated from the Nevzorov and King probes (orange thick line) would suggest that unrimed or slightly rimed aggregates (the best agreement is found with mass-size relations of ; Brown & Francis, 1995, BF95, and the model referred as LS15-B0.1 in ; Leinonen & Szyrmer, 2015, respectively) were sampled for most of the leg. However, with the presence of ice particles larger than $D > 4$ mm, it is likely that the Nevzorov probe underestimates the IWC (Korolev et al., 2013). Another IWC estimate (pink line) which takes into account the degree of riming is computed using mass-size parameters consistent with the fractal shape of ice crystals

obtained from in situ images (parameterization based on ; Heymsfield et al., 2004, data set, hereafter Hal04). This estimate, on the contrary, would indicate that rimed aggregates were present (IWC lying in between LS15-B0.2 and LS15-B0.5 mass-size relations). These comparisons suggest that the in situ probes present on the Citation aircraft during OLYMPEX are not sufficient for quantitatively determining the degree of riming of the ice particles sampled. To this aim, comparison with radar observation will be performed in section 3.2.

3. Forward Modeling of Radar Reflectivity From In Situ Measurements

Before attempting a retrieval, the capability of triple-frequency radar measurements for characterizing microphysics properties can be assessed by comparing the measured reflectivity to the reflectivity modeled from the in situ PSD measurements with different scattering models.

3.1. Electromagnetic-Microphysical Models

To check the consistency between in situ microphysics and triple-frequency radar remote sensing observations, a variety of electromagnetic-microphysical (hereafter EM-MIC) models are introduced in this section. Each of them include a description of the assumed microphysics properties (e.g., particle shape or mass-size relation) and a scattering model. The ice refractive index is determined from Mätzler et al. (2005).

3.1.1. Mie Theory

Early studies modeled ice particles as spheres of homogeneous ice-air mixture (soft sphere model) and used Mie theory (Mie, 1908). While this is accurate enough for dense graupel and hail which tend to have a spherical or conical shape (Battaglia et al., 2014; 2015; Heymsfield et al., 2018), ice particles have a much more irregular shape and more sophisticated representations are needed. While stratiform precipitation such as seen in OLYMPEX does not generally lead to the formation of graupel, the presence of supercooled liquid water may be associated with heavy riming, in particular, when orographic enhancement is active. In order to include this possibility, scattering tables for spherical low-density graupel (hereafter Mie-graupel1) have been produced following the mass-size relation parameters of the lowest-density graupel model shown in Figure 6 and by computing an effective dielectric constant of the ice-air mixture provided by the Maxwell Garnett approximation for elliptical inclusions (Bohren & Huffman, 1983).

3.1.2. T-Matrix

Since ice particles tend to fall with their largest dimension in the horizontal plane, horizontally aligned oblate spheroids with an axial ratio of 0.6 and composed of a homogeneous ice-air mixture (soft spheroid model) have been found to be a much better representation of ice crystals than spheres (Hogan et al., 2012). Since previous studies have found that T-matrix scattering calculations with the Brown and Francis (1995) mass-size relation provides good agreement with radar observations at C, X, and W band (Hogan et al., 2012), scattering tables (hereafter Tmatrix-BF95) are derived from the adaptation of the work of Mishchenko et al. (1996) by Leinonen (2014).

3.1.3. SSRGA

When the particle is significantly larger than the wavelength, several studies (e.g., Botta et al., 2011; Ori et al., 2014; Petty & Huang, 2010; Tyynelä et al., 2011) have shown that methods using simple shapes (like sphere or spheroids) produce backscattering cross sections biased by orders of magnitude compared to methodologies like the discrete dipole approximation (DDA; Draine & Flatau, 1994) that take into account the full details of the ice crystal shape. In addition spherical and spheroidal models cannot account for the full variability of triple-frequency signatures of aggregates (Kneifel et al., 2015; 2016). The Rayleigh-Gans approximation (RGA) and its extension for an ensemble of particles (Self-Similar Rayleigh-Gans Approximation, SSRGA), although very simple in their mathematical formulation and very efficient in the numerical implementation, produce more realistic scattering properties compared to spheres/spheroids models, because they are able to take into account the internal structure of aggregates (Hogan & Westbrook, 2014; Hogan et al., 2017; Tyynelä et al., 2013; Leinonen et al., 2013). SSRGA performs reasonably well—compared to reference methods such as DDA—for lightly and moderately rimed aggregates as well, despite the fact that their higher density might violate some of the prerequisites for the RGA applicability (Leinonen et al., 2018). In this work, the SSRGA is adopted for computing scattering properties of unrimed aggregates using the Brown and Francis (1995) mass-size relation like the soft spheroid model (hereafter SSRGA-BF95), the whole series of model B (initially described in ; Leinonen & Szyrmer, 2015) aggregates with increasing riming (hereafter SSRGA-LS15-Bxx; Leinonen et al., 2018), and dense unrimed aggregates (hereafter Koln17) for which the SSRGA coefficients have been derived following Leinonen and Szyrmer (2015).
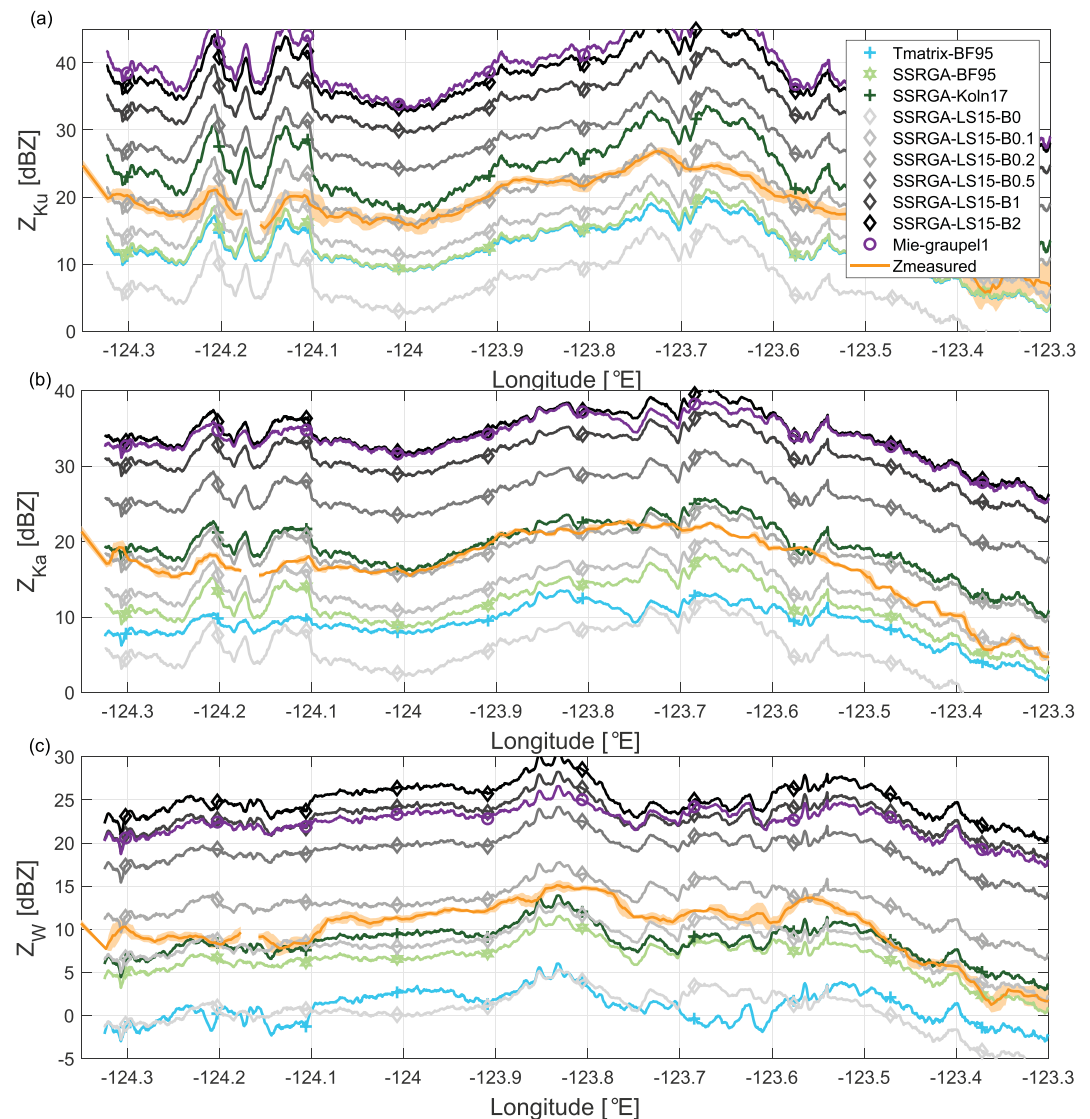
Figure 7. Ku (a), Ka (b), and W band reflectivity (c) observed by the APR-3 at the position of the Citation aircraft (orange lines with shading representing the measurement error) and computed from the observed particle size distribution with some of the mass-size relations of Figure 6 and their associated electromagnetic-microphysical models (see the legend in panel (a) for the line specifications). SSRGA = Self-Similar Rayleigh-Gans Approximation.

3.2. Comparison With Collocated Observed Reflectivity

Figure 7 shows the wide range of reflectivities obtained when applying the different EM-MIC models and different mass-size relations (Figure 6) to the in situ PSD measurements. Comparisons with reflectivities measured by the triple-frequency radar on-board the DC-8 aircraft are made by selecting the closest radar pixels to the Citation aircraft altitude and location after correction for wind advection as described in section 2. Such comparisons indicate which models are the best candidates for matching both the microphysics and scattering properties for this case study.

Ignoring the measured reflectivities in a first instance, some interesting features can already be noticed when looking at results for different EM-MIC models. At Ku band, most of the aggregates behave like Rayleigh scatterers and the soft spheroid model is adequate (Hogan et al., 2017). This is indicated by the overall very good agreement between Tmatrix-BF95 and SSRGA-BF95 (Figure 7a), which uses the same mass-size relation: they differ by less than 2 dB, even when aggregates larger than 9 mm are sampled by the HVPS3 (e.g., in the region around −123.7°E longitude). On the other hand, in comparison with SSRGA, the soft spheroid model leads to a nonnegligible underestimation of reflectivity for higher radar frequencies (between 1 and

5 dB at Ka band and between 3 and 8 dB at W band, in Figures 7b and 7c, respectively). Similarly, in comparison with SSRGA, the soft-sphere model seems to underestimate reflectivity at high frequencies: owing to denser ice particles, the graupel model (Mie-graupel1) results in larger reflectivity than heavily rimed aggregates (SSRGA-LS15-B2) at Ku band, but the opposite is found at W band.

The comparison with measured reflectivities (orange lines) at Ku and Ka bands (Figures 7a and 7b) suggests that this ice cloud is composed of moderately rimed aggregates, as confirmed by CPI particles images of Figure 5a (note that the corresponding particles are small and hence have little contribution to the observed reflectivity; however, only the CPI has a resolution sufficient to clearly diagnose riming which is further corroborated by HVPS3 images of larger particles in Figure 11e). In fact, EM-MIC models of heavily rimed aggregates (SSRGA-LS15-B0.5 and above) clearly overestimate reflectivities by more than 5 dB, while unrimed or slightly rimed aggregates (SSRGA-LS15-B0 and SSRGA-BF95) underestimate them. For most of the leg, the best agreement is found with the SSRGA-LS15-B0.2. This is compatible with the IWC calculations of section 2.2, thus supporting the hypothesis that the Nevzorov probe (AHparam) underestimates (overestimates) IWC in this regime. The results for this leg are in agreement with findings in Chase et al. (2018): the Brown and Francis (1995) mass-size relation does not enable the reproduction of the observed Rayleigh reflectivities for the OLYMPEX campaign and generally leads to an underestimation of Ku band reflectivity. The only difference with Chase et al. (2018) is that they used a soft-sphere model for computing the scattering cross sections but, as previously discussed, this should have a negligible impact at Ku band. On the other hand, the mass-size relations for rimed aggregates used in the SSRGA-LS15-B0.2 model (and which is practically identical to the one proposed in ; Heymsfield et al., 2004) provides much closer agreement generally better than 1 dB, suggesting that the aggregates observed during OLYMPEX were significantly more rimed than those observed in other field campaigns (Hogan et al., 2006; 2012) where the Brown and Francis (1995) mass-size relation was proven adequate. Noticeably, most of their in situ data were sampled in colder conditions (all cases with $T < -10\,°C$ except one where the BF95 mass-size relation also lead to an underestimate of Rayleigh reflectivity).

A closer look at Figures 7a and 7b reveals that around longitudes $-124.22°E$, $-124.12°E$, $-123.65°E$, and for longitudes higher than $-123.55°E$, the observed reflectivities are closer to the SSRGA-LS15-B0.1 model, suggesting small pockets of unrimed snowflakes (zones where riming flag suggests the presence of fluffy aggregates in Figure 3d, as confirmed by particles images of Figure 10). Interestingly, the corresponding reflectivity peaks around $-124.22°E$ and $-124.12°E$ longitudes are also associated with D_m peaks in the in situ PSD with individual particles as large as 10 mm, suggesting the occurrence of aggregation (in Figure 10e, HVPS3 images at $-124.22°E$ confirm the presence of large aggregates). On the contrary, around longitudes $-123.9°E$ (i.e., exactly where the RICE highlights significant icing), the observed reflectivities are a couple of decibels higher than the SSRGA-LS15-B0.2 model, suggesting a region of more rimed particles.

At W band (Figure 7c), the ice cloud and potential liquid water present in between the DC-8 and Citation aircraft can cause significant attenuation of the radar signal. A direct comparison of the reflectivity observed and modeled from the PSD is not as straightforward as that at lower frequencies. The widespread 2- to 5-dB overestimation of reflectivity by the SSRGA-LS15-B0.2 model can be qualitatively explained by attenuation of the radar measurements by the ice itself and by the presence of a thick supercooled liquid water cloud layer, which in turn, is compatible with the observation of rimed aggregates. For a quantitative use of the W band observations, however, a full retrieval combining the multifrequency reflectivity profiles such as in Battaglia, Mroz, Lang, et al. (2016) is necessary in order to disentangle the scattering and attenuation effects.

4. Retrieval Algorithm

The previous section showed that multifrequency radar observations can provide insights on the degree of riming of ice particles. A more quantitative assessment can be drawn by exploiting the outputs of the retrieval algorithm developed in this study. It is based on optimal estimation (Rodgers, 2000), which has been already successfully applied in the area of cloud and precipitation remote sensing (e.g., by Battaglia, Mroz, Lang, et al., 2016; Battaglia, Mroz, Tanelli et al., 2016; Delanoë & Hogan, 2008; Grecu et al., 2011; Mace et al., 2016; Mason et al., 2017; Mason et al., 2018; Munchak & Kummerow, 2011; Tridon & Battaglia, 2015; Tridon et al., 2017). While multifrequency radar observations are the backbone of this retrieval methodology, it can also easily assimilate vertically integrated information such as the path integrated attenuation (PIA) such as in Battaglia, Mroz, Lang, et al. (2016). These parameters are obtained from the surface reference technique.

Since the reflectivity of land-covered surfaces are not easily estimated, the version of the retrieval which includes PIA (hereafter, RetZPIA) is only aimed at retrievals over ocean, while only reflectivity profiles are used over land (hereafter, RetZ).

The general inverse problem consists of retrieving an unknown state vector $\mathbf{x}$ from a measurement vector $\mathbf{y}$ affected by a measurement error $\mathbf{\epsilon}$, that is, $\mathbf{y} = \mathbf{F}(\mathbf{x}) + \mathbf{\epsilon}$ where $\mathbf{F}$ represents a forward operator mapping state into measured variables. The retrieval problem is solved by minimizing the cost function:

$$CF = \underbrace{[\mathbf{y} - \mathbf{F}(\mathbf{x})]^T \mathbf{S}_\epsilon^{-1} [\mathbf{y} - \mathbf{F}(\mathbf{x})]}_{CF_{\text{meas}}} + \underbrace{[\mathbf{x} - \mathbf{x}_a]^T \mathbf{S}_a^{-1} [\mathbf{x} - \mathbf{x}_a]}_{CF_{\text{a priori}}} \tag{6}$$

where $\mathbf{S}_\epsilon$ is the measurement error covariance matrix, $\mathbf{x}_a$ is the *a priori* value of $\mathbf{x}$, and $\mathbf{S}_a$ the associated covariance matrix. The solution can be found by Newtonian iterations based on the Gauss-Newton method (Rodgers, 2000).

The present retrieval technique is tailored for stratiform precipitation and is applied profile by profile. In such a configuration, the measurement vector combines reflectivity profiles with PIA measurements, while the unknown vector is composed of parameters allowing to characterize the profile of hydrometeors. Details are given in the following subsections, along with further considerations on the a priori and forward model used in the retrieval.

4.1. Unknowns

Stratiform precipitation is characterized by the presence of a clear melting layer that marks the transition between the solid and liquid phases. The top and bottom of the melting levels are identified by exploiting the characteristic bright band features in the lowest radar frequency available (Ku band) as proposed by Fabry and Zawadzki (1995). Correspondingly, ice (rain) particles are retrieved only above (below) the bright band. At the moment, situations with double band occurrences (Emory et al., 2014) are not handled by the algorithm.

The retrieved rain and ice characteristics are described by PSDs. As proposed by Testud et al. (2001), rain PSDs are well represented by Gamma distributions $N(D) = N_0 D^\mu e^{-\lambda D}$ where N_0, μ, and λ are the concentration, shape, and lambda parameters, respectively, and $\lambda = (4 + \mu)/D_m$. As mentioned in section 2.2, an exponential distribution (i.e., with $\mu = 0$) seems to represent ice in situ PSDs reasonably well for this case study. As shown by Mason et al. (2019), such an assumption may have a nonnegligible impact on the retrievals but the choice here is made to limit the number of unknowns. For the same reason, a relation between the rain mean mass diameter, D_m (equation (3)), and the rain mass spectrum standard deviation, σ_m (equation (5)), of the rain PSD is used following (Williams et al., 2014; see section 4.2), and the shape parameter μ of the Gamma function is then derived according to

$$\mu = \left(\frac{D_m}{\sigma_m}\right)^2 - 4. \tag{7}$$

The PSDs are therefore fully defined with two parameters, such as the equivalent water content (WC) and the mean mass diameter (D_m), chosen for their simple physical interpretation. Accordingly, *the state vector* is

$$\mathbf{x}^T = \left(\underbrace{D_m^i[1] \ldots D_m^i[N_i] \log\left(IWC[1]\right) \ldots \log\left(IWC[N_i]\right)}_{\text{ice}} \underbrace{D_m^r[1] \ldots D_m^r[N_r] \log\left(LWC[1]\right) \ldots \log\left(LWC[N_r]\right)}_{\text{rain}} \underbrace{\alpha'_{ML}(Ku)\alpha'_{ML}(Ka)\alpha'_{ML}(W)}_{\text{melting}} \right) \tag{8}$$

where ice and rain are hydrometeors defined on a different number of levels (respectively, N_i and N_r) as defined by the a priori (see discussion below). The parameters α_{ML}' are used to characterize the attenuation of the melting layer at the different frequencies (see the discussion in section 4.3). Since the WC can vary over wide intervals, its logarithm is taken in order to avoid the occurrence of nonphysical negative values.

While thick liquid clouds can produce substantial attenuation at W band, they are very challenging to detect with any radar. In this study, it is not attempted to retrieve supercooled liquid water (SLW) clouds because it is not clear if the triple-frequency radar profiles really have enough information content. However, since
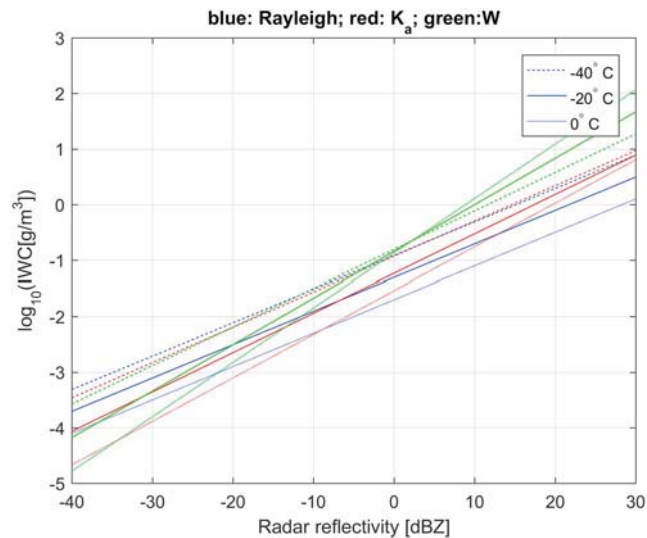
Figure 8. Empirical formula relating ice water content (IWC) to temperature and Z_e measured by a Rayleigh (blue), Ka (red), and W band (green) radar from Hogan et al. (2006) and Protat et al. (2007).

SLW should be spatially correlated with riming, it is important to assess its effect on the retrieval accuracy. Therefore, two versions of the retrieval will be conducted:

- a control version for which supercooled water is assumed negligible (probably adapted to most of the flight since the RICE detected SLW for short periods only);
- another version using the median supercooled liquid water for that day (with LWC ranging from 0.01 at 7 km and 0.04 g/m³ at 3 km) as measured by the King hot wire probe (for more details, see Chase et al., 2018).

Section 5 will focus mainly on the results of the control version and the differences between both versions will be described in section 5.4.

4.2. A Priori for Snow and Rain Microphysics

Since WC and Dm are very variable, it is not straightforward to provide an a priori on their profile and a climatological average would be a very poor constraint. Therefore, even if the a priori should not depend on the observations, a single-frequency retrieval is used as mean prior following L'Ecuyer and Stephens (2002). In order to limit an implicit overweighting to that reflectivity profile, it is associated with a very large a priori error. The a priori IWC profile is based on temperature-dependent *Z-IWC* relationships reported by (Hogan et al., 2006 and Protat et al., 2007; their midlatitude relation) for Rayleigh and Ka-W band frequencies, respectively, and here illustrated in Figure 8. The lowest frequency available is used to estimate the a priori profile, that is, Ku in the current case. The variance is assumed to change according to Protat et al. (2007), who have thoroughly investigated errors related to *Z-IWC* relationships.

The a priori ice D_m profile is then derived based on the a priori IWC and on the assumed EM-MIC model. Since a single-wavelength radar method does not fully constrain the ice microphysics—in particular the ice crystal size—a large error is allowed (the smallest between 50% of the diameter and 1.5 mm).

The a priori rain parameters and their variance are derived from the reflectivity profile at the lowest frequency (assumed to be nonattenuated). More than 200,000 1-min samples of disdrometer observations from various NASA ground validation field campaigns between 2011 and 2016 (for more information on the data set, see D'Adderio et al., 2018) provide climatological properties (Figure 9), allowing the derivation of relations between reflectivity at Ku Z_{Ku}, the rain D_m, and the mass spectrum standard deviation σ_m of the rain PSD (Figure 9). From these relations, a priori profiles of D_m and σ_m, and then μ are derived. The D_m obtained via this methodology is associated with a large standard deviation because the relation between Z_{Ku} and D_m may depend on the type of rainfall, in particular at large D_m (Figure 9a). On the other hand, D_m and σ_m are known to be highly correlated (Williams et al., 2014). With the Gamma shape of the PSD fully constrained
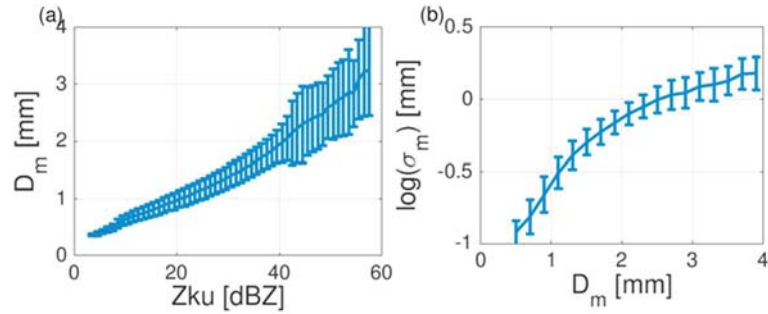
Figure 9. (a) Mean and standard deviation of mean mass diameter D_m per bin of reflectivity at Z_{Ku} and (b) mean and standard deviation of the logarithm of the rain PSD mass spectrum standard deviation σ_m per bin of D_m, for a data set of more than 200,000 drop size distributions collected during the NASA GPM ground validation field campaigns. PSD = particle size distribution; NASA = National Aeronautics and Space Administration; GPM = Global Precipitation Measurement.

by D_m and μ, absolute concentration of drops is obtained by matching the observed reflectivity (still at the lowest frequency), and Rain Water Content (RWC) can be finally derived from the resulting PSD.

4.3. Melting Layer

In stratiform precipitation, the layer where ice particles melt appears as a bright band at low radar frequency. The peak intensity of the bright band tends to decrease considerably for millimeter radars as a combined effect of attenuation and non-Rayleigh effects (Kollias & Albrecht, 2005). Because of the complexity in modeling the backscattering of melting particles, a pragmatic approach is here adopted: the radar reflectivity measurements within the melting layer are not used and thus are not fitted by the forward model. On the other hand, the total extinction of the melting layer, which affects the radar attenuation, is parameterized as a function of the rain rate below the bright band. Following Matrosov (2008) and assuming that the extinction coefficient is constant over the melting layer, it is proportional to the rain extinction just below the melting layer according to

$$k_{\text{ext}}^{\text{ML}}[\text{dB/km}] = \alpha_{\text{ML}}(f)\, k_{\text{ext}}^{\text{rain}}[\text{dB/km}] \tag{9}$$

where $\alpha_{\text{ML}}(f)$ is frequency dependent. These are crude assumptions, but they are believed to provide a very good first-order approximation to the problem. The values of α_{ML} for Ku, Ka, and W band are three additional unknown parameters; their values are allowed to vary in a range $[\alpha_1(f) : \alpha_2(f)]$ which is provided by experimental and theoretical predictions (Matrosov, 2008). Such range is assumed to be [2:6], [2:5], and [1:3] for Ku, Ka, and W band, respectively. Instead of using $\alpha_{\text{ML}}(f)$, a new variable $\alpha\text{ML}'(f)$ is included in the state vector (equation (8)):

$$\alpha'_{ML}(f) = \tan\left[\pi\left(\frac{\alpha_{ML}(f) - \alpha_1(f)}{\alpha_2(f) - \alpha_1(f)} - 0.5\right)\right] \tag{10}$$

which has the advantage of not being bounded. The mean a priori for such variable corresponds to the center of the range interval with a variance assumed to be equal to one.

4.4. Measurements

The *measurement vector* is a combination of radar reflectivities and PIAs in the following form:

$$\mathbf{y}^T = \left(Z_m^{Ku}[r_1]\dots Z_m^{Ku}[r_{N_{Ku}}]\; Z_m^{Ka}[r_1]\dots Z_m^{Ka}[r_{N_{Ka}}]\; Z_m^{W}[r_1]\dots Z_m^{W}[r_{N_W}]\; \delta PIA^{Ku-Ka}\; PIA^{W}\right) \tag{11}$$

where the measured reflectivities have been resampled at the same ranges $r_1, \dots, r_S$. Reflectivity errors are computed according to the signal-to-noise ratio with standard deviation errors reaching 0.5 dB (1.0 dB) at large signal-to-noise ratios for Ku/Ka (W band).

PIAs are estimated only over water by using the surface reference technique (Meneghini et al., 2012). The estimate of the measured σ_0 is obtained by integrating the reflectivity of the reflectivity peak (see Battaglia
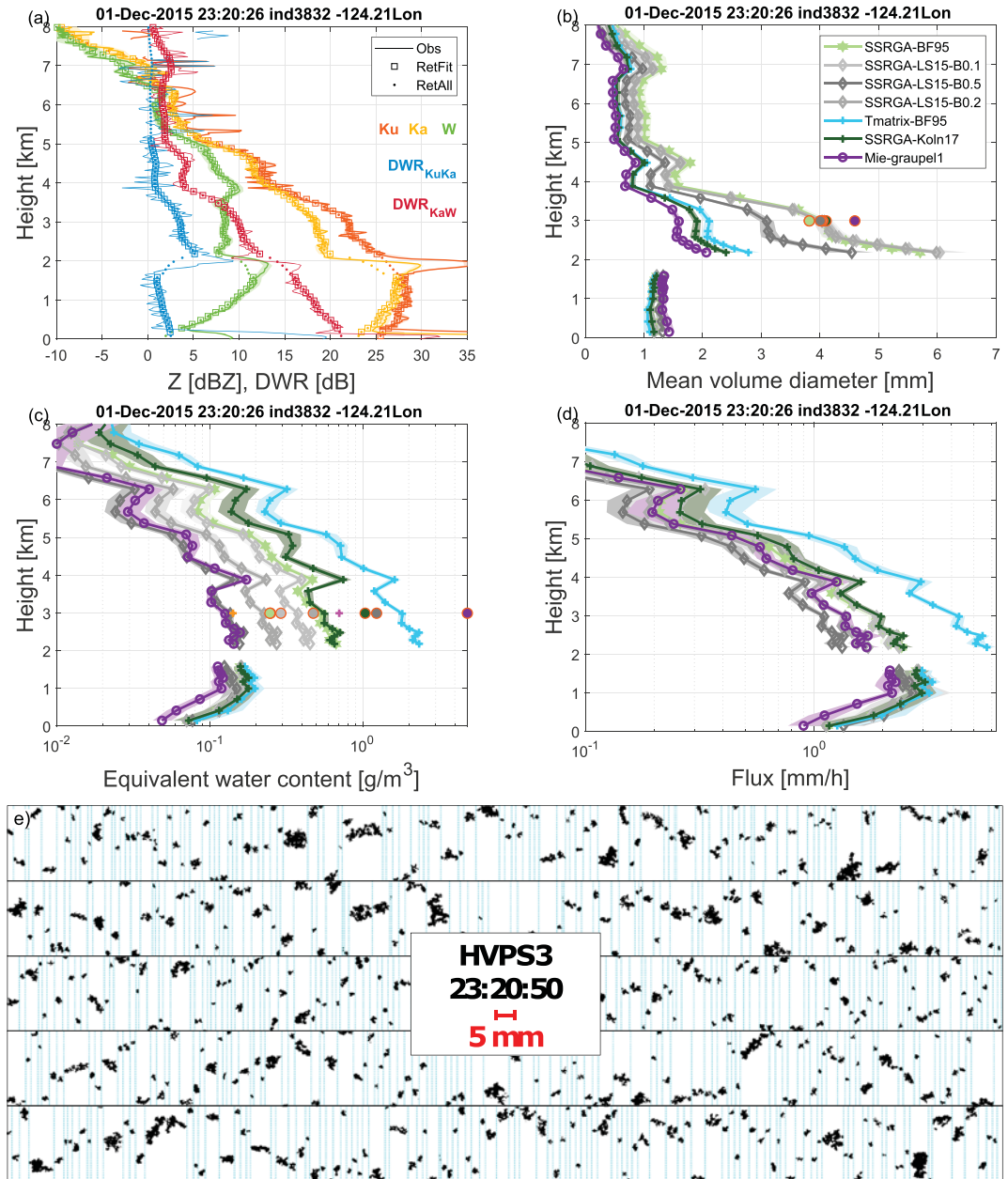
Figure 10. Profiles of observed Ku, Ka, W reflectivity, and corresponding Ku-Ka and Ka-W dual wavelength ratios (DWRs) in dark orange, orange, green, blue, and magenta, respectively (a), retrieved D_m (b), WC (c), and corresponding flux (d) at $-124.21°$E during the more effective aggregation period. Shadings show the retrieval error. The collocated in situ D_m and WC are indicated by colored disks (following the color code of the legend in Figure 4c) and the corresponding images of the ice crystals are shown in panel (e). WC = water content; SSRGA = Self-Similar Rayleigh-Gans Approximation.

et al., 2017) while the effective σ_0 is computed from the surface wind. Errors of 0.5 dB have been assumed for PIAs. Errors on PIAs and reflectivities at different range gates are assumed to be independent so that the measurement error covariance matrix can be written in the block diagonal form:

$$S_\epsilon = \begin{bmatrix} S_Z & 0 \\ 0 & S_{\text{PIA}} \end{bmatrix} \tag{12}$$

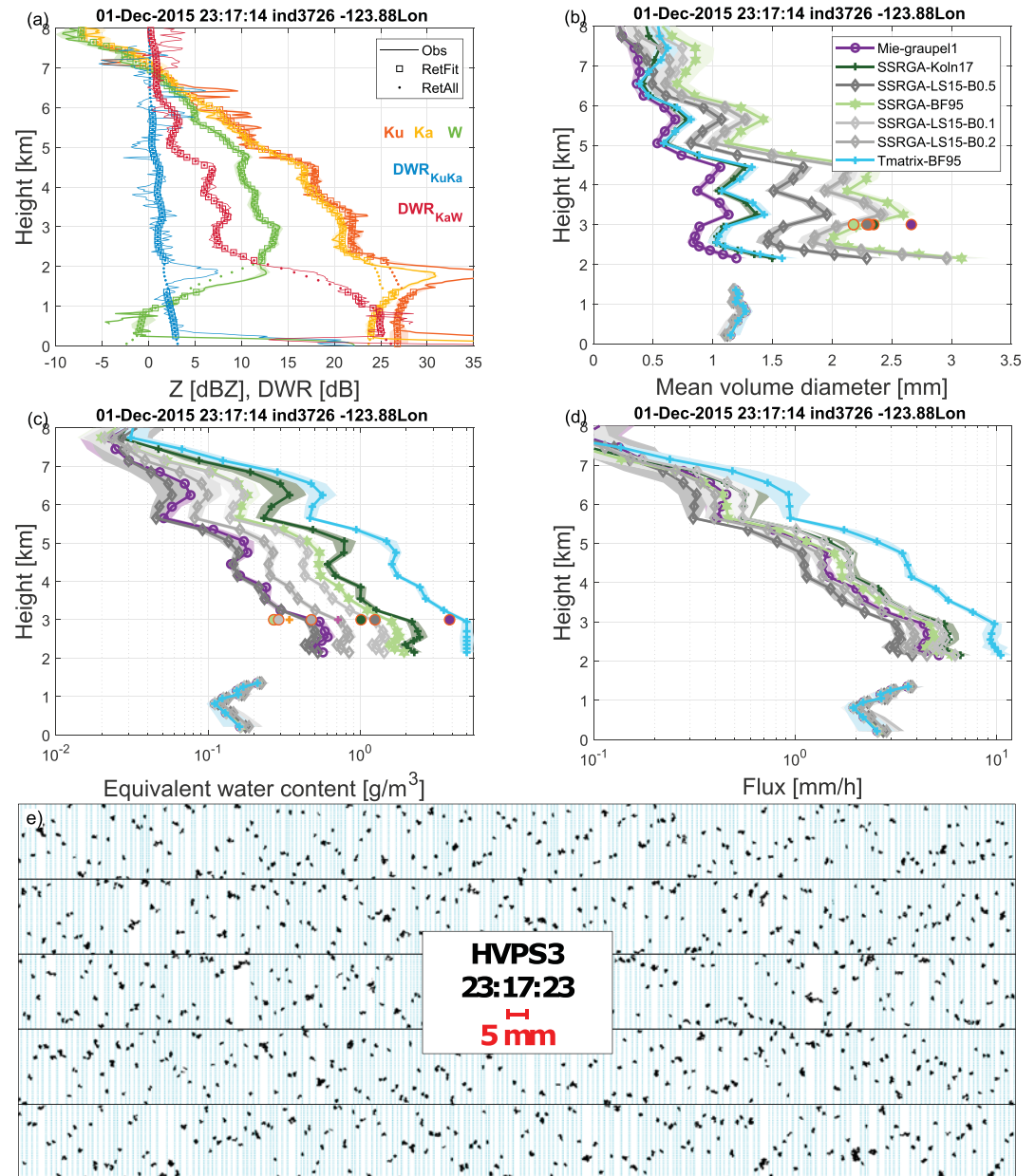where S_Z and S_{PIA} are diagonal matrices.

Figure 11. Same as Figure 10 at $-123.88°$ E during a more effective riming period. DWR = dual wavelength ratio; SSRGA = Self-Similar Rayleigh-Gans Approximation.

4.5. Forward Model

Following the methodology of the rain a priori determination, the high correlation between D_m and σ_m (Figure 9b) is exploited to derive σ_m and then the μ parameter according to equation (7), which allows the definition of the whole Gamma PSD of rain, while the exponential ice PSD is fully determined by D_m and IWC.

Look-up tables of backscattering and extinction cross sections are obtained from T-matrix calculations for rain. The refractive index of water is computed following Ray (1972) for different temperatures. The single scattering properties of the raindrops are derived from T-matrix computations (Mishchenko, 2000). For ice particles, all the methods described in section 3.1 are used, each for independent retrieval attempts.

Finally, the code developed in Hogan and Battaglia (2008) is adopted as forward operator for computing the reflectivity profiles, the PIAs and, via the perturbation method, the relevant Jacobians.

5. Retrieval Results

The control version of the retrieval (i.e., neglecting the presence of SLW) is applied, profile by profile, to the multifrequency radar observations of the full transect described in section 2.1 and includes PIAs for the part which is over the ocean (between −125 and −124.23°E). Detailed retrievals are first presented in section 5.1 for two profiles representative of periods with more effective aggregation and riming (−124.21 and −124.03°E in Figures 10 and 11, respectively, as identified in Figure 7) and where colocated in situ observations of ice are available. Coincidentally, the Citation aircraft descended through the melting layer when passing over the coast (see Figure 3d) and both profiles are therefore over land where PIAs cannot be included in the measurement vector. The retrieval over the full transect is then shown in section 5.2 and compared with in situ observations of both ice and rain layers in section 5.3. Results of the retrieval version including SLW are discussed in section 5.4.

5.1. Example of Specific Profiles: Aggregation Versus Riming

Both reflectivity profiles (Figures 10a and 11a) are typical of stratiform precipitation with

- the upper part of the cloud (above 6.5 km) composed only of small particles which scatter the three radar wavelengths in the Rayleigh regime (all three reflectivities are identical);
- a reflectivity peak at Ku band (around 2 km) corresponding to the melting layer; and
- a slightly decreasing reflectivity at Ku and Ka band in the rain layer below with a stronger decrease at W band due to rain attenuation.

Within the 6.5- to 2-km layer, the Ku-Ka and Ka-W DWRs (blue and magenta lines in Figures 10a and 11a) gradually increase toward the ground, a signature of the increase of the non-Rayleigh scattering of the ice aggregates. On the other hand, the two profiles differ below 3.5 km: while they present a similar DWR_{Ka-W} of about 8–10 dB, a larger DWR_{Ku-Ka} is noticeable in the case of aggregation. This behavior agrees with previous studies on triple-frequency radar observations (e.g., Kneifel et al. (2015)).

The retrieval is applied to these two profiles using the various EM-MIC models discussed in section 3.1. The retrieved D_m, WC, and corresponding mass flux profiles which best fit the measurement are shown in Figures 10b, 11b, Figures 10c, 11c, and Figures 10d, 11d, respectively. Color shadings indicate the retrieval errors for each EM-MIC model. No forward model error is considered, because it is already represented by the differences between each retrieval attempt. Errors on mass flux are derived via Monte Carlo propagation of D_m and IWC errors assuming that they follow normal and lognormal distributions, respectively. While all the retrieval attempts are converging to a similar solution in rain (note that this solution may be dictated by the prior assumption on D_m and RWC which is the same for all attempts), the retrieved ice D_m and IWC span a large range of values, depending on the EM-MIC model being used.

The retrievals are compared with the closest in situ observations derived from the PSD (disks at 3 km), using the corresponding mass-size relations (according to the color of the disk). Since D_m derived from in situ measurements barely depends on the mass-size relation, it is a good constraint to identify the EM-MIC model leading to the best solutions. Several EM-MIC models (SSRGA-BF95, SSRGA-LS15-B0.1, and SSRGA-LS15-B0.2) provide consistent radar-retrieved and in situ estimates of D_m. This suggests that those three models provide a good match of measured DWRs. In order to match the WC, they mainly require to be associated with the correct mass-size relation. In agreement with the reflectivity comparison in Figure 7, the best models that lead to a consistent retrieved D_m and in situ WC are SSRGA-LS15-B0.1 and SSRGA-LS15-B0.2 for the profile with more effective aggregation and more effective riming, respectively.

Assuming a negligible vertical wind, the precipitation flux can be derived from the retrieved D_m and WC profiles using the $v_t(D)$ relation associated with each ice model. Terminal fall velocities of ice aggregates are difficult to observe and are fairly uncertain, but interestingly, the solutions in agreement with in situ measurements present a good continuity between the ice and rain layers (flux increasing from 2 to 2.6 mm/hr and decreasing from 4.2 to 3.6 mm/hr in Figures 10d and 11d, respectively). Note, however, that, as shown in the next section, this is only valid for retrievals which are done for the over land part of the flight transect. Finally, the corresponding images from the HVPS3 probe confirm the presence of larger aggregates with a very fluffy structure during the aggregation period, while smaller particles with practically spherical shapes are found during the riming period (Figures 10e and 11e, respectively).
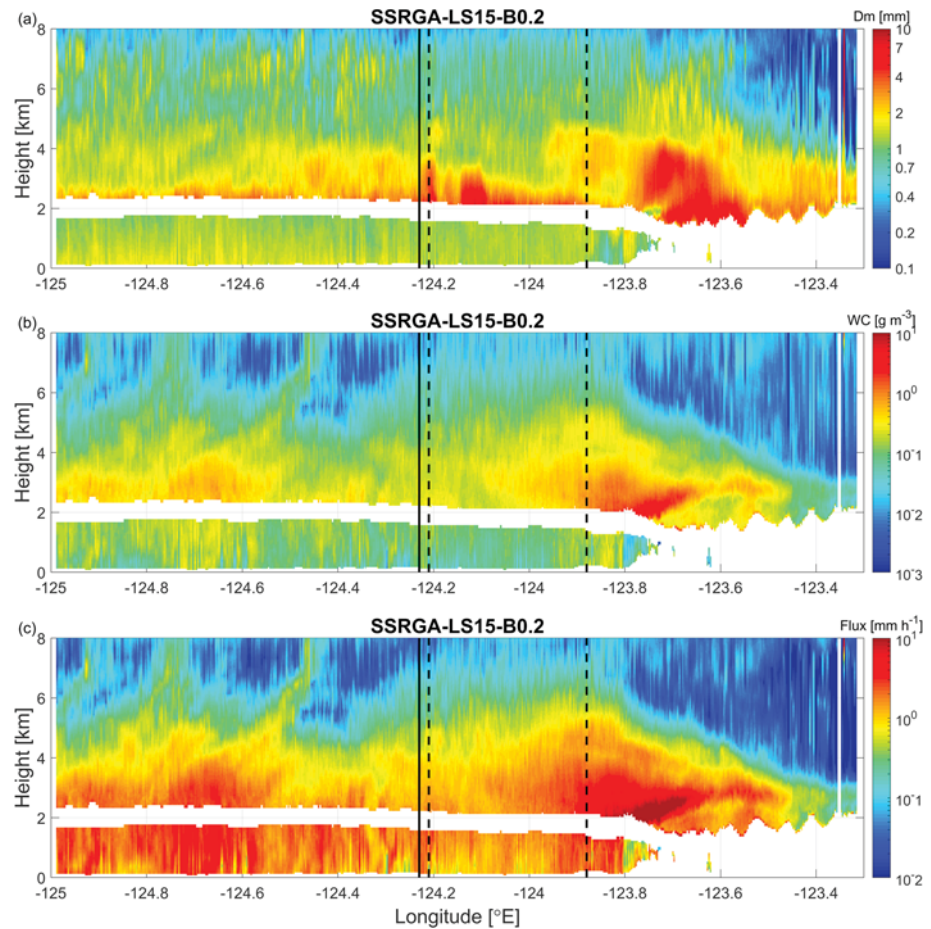
Figure 12. Time-height fields of the retrieved D_m (a), WC (b), and flux (c) with the SSRGA-LS15-B0.2 model. In each panel, the continuous black line separates the retrievals made over land (to the east) and over ocean (to the west), and the dashed black lines show the position of profiles presented in Figures 10 and 11. WC = water content; SSRGA = Self-Similar Rayleigh-Gans Approximation.

5.2. Retrieval Over the Full Leg

The retrieval is then applied to the full leg of radar observations using the different EM-MIC models. As the SSRGA-LS15-B0.2 model was found to describe the properties of ice for most of the transect, the corresponding retrieved time-height evolutions of D_m, WC, and water mass flux are shown in Figure 12. While the retrieval is applied to each profile independently, the retrieved fields present a realistic and coherent structure. Two active aggregation periods are evident, with a WC lower than 0.3 g/m^3 and D_m reaching 6 and 8 mm at -124.21 and $124.12°$E, respectively. On the other hand, for most of the transect, WC can reach significantly larger values with D_m remaining smaller than 2 mm.

While the retrieved rain properties are continuous over the full transect when only reflectivities are used (not shown), a clear discontinuity (continuous black line at $-124.23°$E) appears at the transition from land to ocean when PIAs are used over the ocean. While rain evaporation may be more important over land, such sharp and strong differences in rain properties are questionable, in particular for RWC with a decrease of almost an order of magnitude. More plausible explanations are that the retrieval including PIAs is indeed better constrained and converge to a better solution, or there is inconsistency between reflectivity profiles and PIAs and this pushes the solution in a different direction compared to the radar-only solution. However, while the mass flux looks consistent between the ice and rain layers over land (as it was found in Figures 10d and 11d), the rain rate is significantly larger over the ocean. As will be further discussed in section 5.5), one explanation could be that the terminal fall velocity of ice aggregates and/or rain drops are not well parameterized.
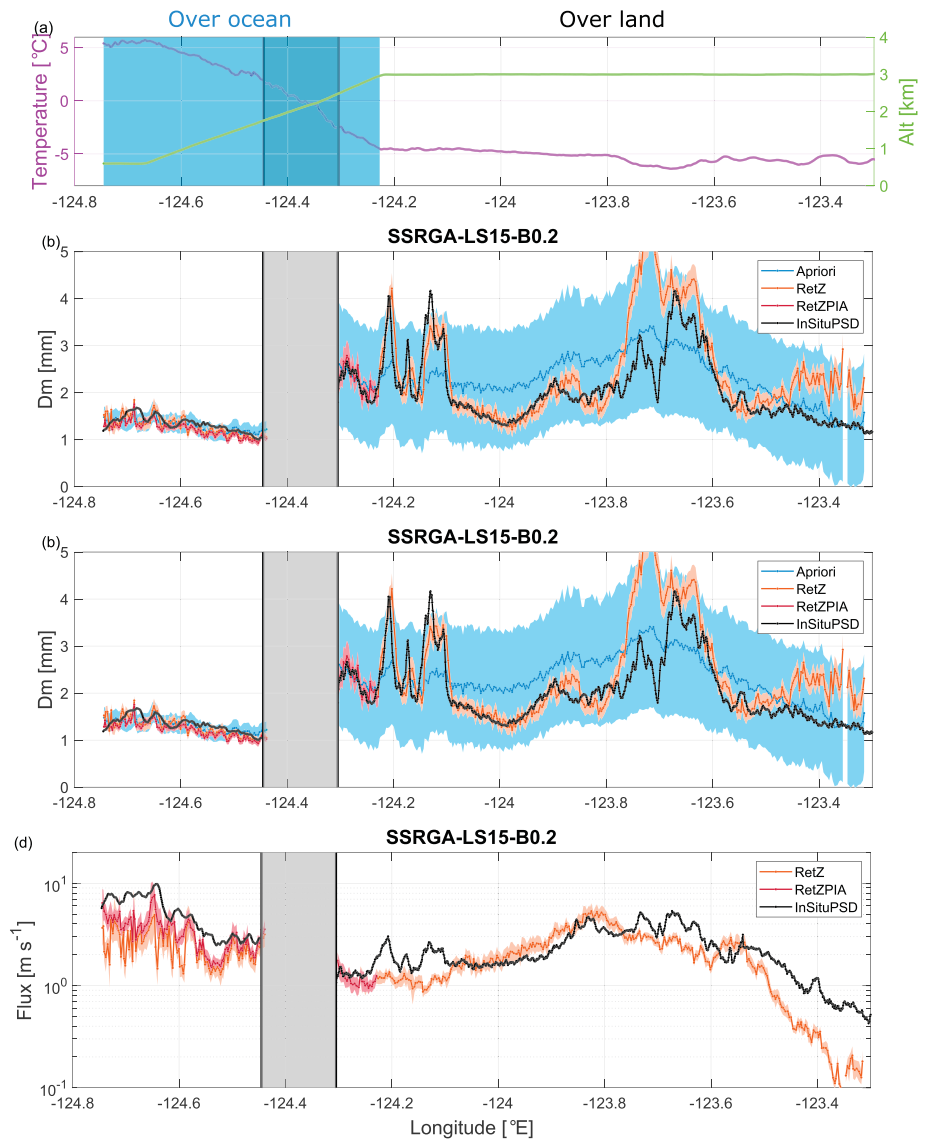
Figure 13. (a) Temperature and altitude of the in situ observations along the full Citation leg on which are compared the in situ (black line), a priori (blue line and shading), and retrieved (red and dark orange lines and shadings) D_m (b), WC (c), and mass flux (d). Also shown in panel (b) are the WC estimated from the Nevzorov probe (orange line) and Hal04 estimate (pink line). The LS15-B0.2 ice model is used both in the retrieval and for computing the parameters from the in situ PSD. SSRGA = Self-Similar Rayleigh-Gans Approximation; WC = water content; PSD = particle size distribution.

5.3. Comparison With In Situ

In situ observations along the full Citation leg (including both rain and ice part over land or ocean, see Figure 13a) are compared with D_m, WC, and mass flux retrieved with the SSRGA-LS15-B0.2 ice model in Figures 13b–13d, respectively. Over ocean, the retrieval versions with (RetZPIA) and without (RetZ) PIAs are shown. For the small portion of ice observations over ocean (between −124.3 and −124.23°E), only the former version is visible on the plots (red line) because both versions are identical. It is not surprising because the rain and melting layer have the largest influence on PIAs. Indeed, assimilating PIAs could be certainly beneficial for ice retrievals, but only if the rest of the profile is retrieved with high accuracy.

For rain, the retrieval of D_m is well constrained by DWRs and the a priori is already in good agreement with in situ measurements. On the other hand, the a priori largely underestimates the WC. While the retrieval using reflectivities only (RetZ) cannot counteract this underestimation and appear very noisy, the assimilation of
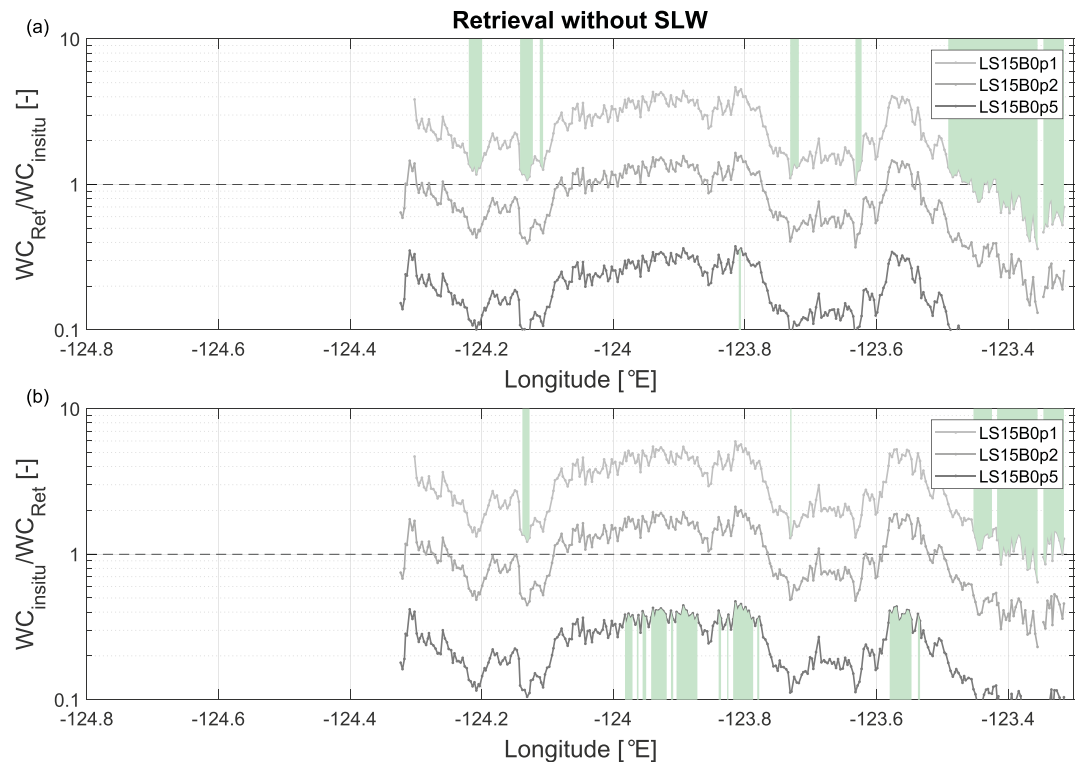
Figure 14. Ratio between in situ and retrieved IWC using different EM-MIC models for the ice part of the Citation leg for retrieval versions without (a) and with (b) supercooled liquid water. In each case, the corresponding ice model is used for computing the in situ IWC. Green shadings show periods where the LS15-B0.1 or the LS15-B0.5 ice models provide better results than LS15-B0.2. IWC = ice water content; EM-MIC = electromagnetic-microphysical; WC = water content; SLW = supercooled liquid water.

PIA (RetZPIA) leads to a slightly improved RWC when compared with in situ measurements, at the expense of a slightly worse D_m.

For ice, the a priori (blue line with shading indicating the a priori error) shows an overall reasonable agreement, even if it is not capable of reproducing small-scale variability such as the D_m peaks at −124.21 and 124.12°E. The agreement is improved over the full leg for the retrieved D_m (dark orange line), and in some parts for the retrieved IWC, in particular between −123.9 and 124.1°E. Furthermore, in agreement with the results of section 3.2, the IWC is overall underestimated by the Nevzorov probe (orange line) and overestimated by the Hal04 parameterization (pink line).

In the regions where particles have undergone more effective aggregation and riming, the IWC retrieved with the SSRGA-LS15-B0.2 is underestimated and overestimated, respectively. The agreement can actually be improved (green shading periods in Figure 14a) when using an ice model corresponding to less and more rimed aggregates, respectively. For example, the SSRGA-LS15-B0.1 model provides a better agreement in the effective aggregation regions (−124.21 and −124.12°E) and for longitudes larger than −123.47°E. Note that the IWC derived from in situ also depends on the ice density model used, as was shown in Figure 4.

5.4. Impact of the Presence of Supercooled Liquid Water on the Retrieval

The version of the retrieval with some SLW leads to slight changes in the ice part. Because of larger attenuation due to cloud liquid water at W band, the DWR_{Ka-W} due to snow is reduced, which leads to a slightly smaller retrieved D_m, which must be compensated by a slightly larger IWC in order to match the absolute reflectivities (not shown). Except for areas near the mountain range, this new version of the retrieval gives overall a slightly worse fit in terms of agreement with the observed in situ D_m (not shown). In terms of IWC, with a IWC_{Ret}/IWC_{insitu} ratio shifted toward larger values by about 1 dB (see Figure 14b), the results depend on the chosen EM-MIC model: while the agreement is overall slightly worse with SSRGA-LS15-B0.2, interestingly SSRGA-LS15-B0.5 gives more often a best agreement near the mountain range (between −124 and −123.8°E). These results are consistent with the idea that the part of the system where rimed particles are
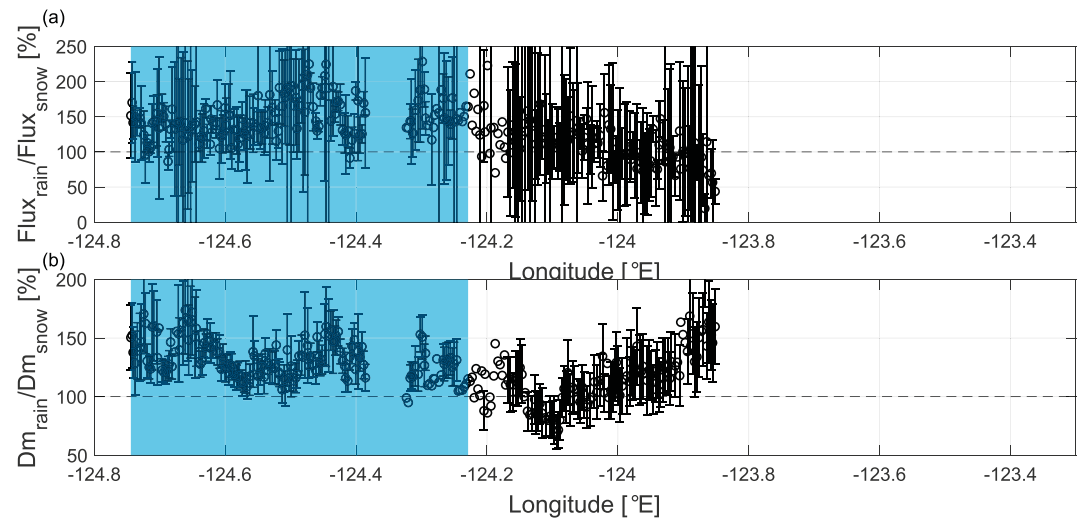
Figure 15. (a) Ratio between the rain flux and snow flux retrieved just above and below the melting layer. (b) Ratio between the rain D_m and the snow melted D_m retrieved just above and below the melting layer.

found is also likely to contain more SLW. However, a full retrieval of ice properties and SLW remains a complex unconstrained problem. This comparison shows that, while SLW cannot be neglected, its impact on the retrieval of WC and D_m is limited. Therefore, only the control version of the retrieval will be further analyzed.

5.5. Flux Continuity Within the Melting Layer

This work emphasizes that ice retrievals are challenging even when high-quality and high-resolution triple-frequency radar observations are available. In order to improve ice retrievals in stratiform precipitation when fewer or lower-quality observations are available (e.g., with GPM measurements), additional constraints are highly desirable. One possibility is to link the ice properties to the retrieved rain properties below the melting layer and exploit conservation of the mass flux (Bennartz & Petty, 2001; Heymsfield et al., 2018) and the potential continuity of the melted mean mass diameter within the melting layer. The range of validity of such conservation constraints, however, depends on the relative humidity and on complex processes such as the aggregation efficiency within the melting layer. Even if the parameterizations of the processes involved are still uncertain, Heymsfield et al. (2018) show from theoretical simulations that in saturated conditions the mass flux can increase by 10% due to accretion of liquid water, while in subsaturated conditions the mass flux can decrease by as much as 25% due to sublimation and evaporation.

Since the present study retrieves the properties of the ice and rain layers independently, it gives the opportunity to investigate this concept by computing the ratio between the retrieved rain and ice mass flux (Figure 15a), and rain and melted ice mean mass diameter (Figure 15b). The first pixels above and below the melting layer are used for computing the mass flux and D_m ratios. For this analysis, the best configuration of the retrieval is chosen, that is, the control version using PIAs over ocean (as in Figure 12). Results are shown only for longitudes lower than $-123.85°$E in order to avoid the mountain range which is susceptible to complex dynamics (see Figures 3a). The errors on the mass flux and D_m ratios are derived via the propagation of errors assuming that they are independent. Even if the uncertainty of the relation between ice crystals fall speed and diameter is not taken into account, the error on mass flux is fairly large. Therefore, it is not surprising that the mass flux ratio is noisy, which certainly limit the potential of using such a constraint. Nevertheless, the majority of points are included between 100 and 200%, that is, much larger values than what is expected by theory. Similarly, the mass flux computed from in situ PSDs—using the same parameterization for the ice crystal fallspeed—is on average significantly larger in rain than in ice (see Figure 13c), suggesting that this is not a retrieval issue. A possible explanation is that the terminal fall velocity of ice aggregates might be underestimated. As in Figure 12, the discontinuity at $-124.23°$E is due to the use of PIAs over ocean. While the retrieved values should be less accurate over land, they are closer to the expected range (between 100% and 150%). However, this could simply be a coincidental consequence of the simultaneous underestimation of ice terminal fall velocity and rain water content (as suggested by Figure 12b).
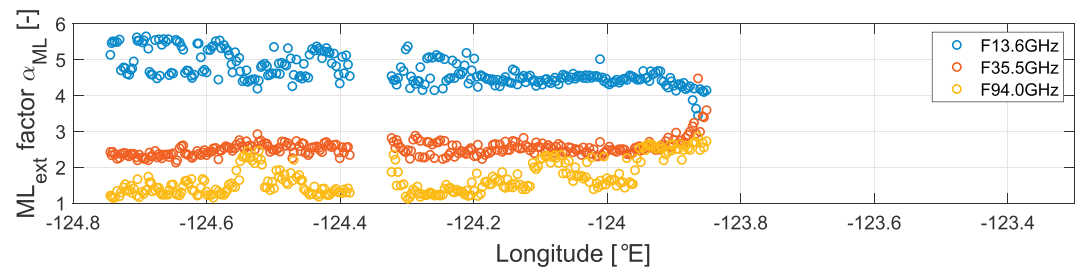
Figure 16. Melting layer extinction factor α_{ML} (as defined in equation (9)) at Ku, Ka, and W band.

For most of the transect the melted mean mass diameter increases through the melting layer (most of the points in Figure 15b are included between 100% and 160%), which can be easily explained by a dominance of aggregation versus breakup processes within the melting layer. On the other hand, the few occurrences of large unrimed aggregates (−124.21 and 124.12°E) are actually associated with a decrease of the melted mean mass diameter by 20%. This is consistent with modeling results from Leinonen and von Lerber (2018), where large aggregates are found more likely to fragment into multiple droplets while melting.

5.6. Melting Layer Attenuation

It is important to take into account the melting layer attenuation when retrieving precipitation properties from millimeter-wavelength radars. For example, it can produce a nonnegligible reduction of ice clouds reflectivity observed by ground-based radars. Conversely, it can be a significant contribution to the PIA used in spaceborne radar rain retrievals like GPM.

The current retrieval assumes a proportionality factor α_{ML} between the melting layer extinction and the rain extinction just below the melting layer. At Ka band, α_{ML} is found to be close to 2.5 (Figure 16), in agreement with Matrosov (2008). At Ku and W band, the proportionality factors tend to change more broadly with values in the range [4.5–5.5] and [1–2.5], respectively, a slightly reduced range compared to what was assumed in the a priori (section 5.6). Note that the retrieved α_{ML} at Ku band appears to jump between two solutions over time, though this corresponds to a very small difference of 0.2 dB in two-way path attenuation. The large W band variability can be ascribed to other effects, for example, the additional presence of cloud water within the melting layer which will significantly contribute to the attenuation of the layer. While the description of the melting layer attenuation is certainly very crude, this is the first attempt to parameterize such effect on triple-frequency measurements. More thorough studies (likely based on long-term ground-based observations) are needed to better address this problem.

6. Conclusions

Accurate microphysical characterization of condensed water in stratiform precipitation systems is crucial for understanding and thus predicting their evolution and for properly quantifying associated precipitation rates. This study combines remote sensing observations from airborne multifrequency radars with airborne in situ observations taken during the GPM ground validation OLYMPEX/RADEX field campaign. For this campaign, the in situ measurements of the IWC were subject to large uncertainties, and therefore various mass-size relations are used to estimate the IWC from the particle size distribution. Furthermore, the corresponding radar reflectivity is computed using various scattering models, namely, the Mie theory, the T-matrix method, and the SSRGA. In particular, the association of SSRGA with various mass-size relations emphasizes the importance of ice crystals density for the calculation of radar reflectivity. At millimeter-wavelength (Ka and in particular W bands), the Mie theory leads to an underestimation of radar reflectivity. When SSRGA is used, the resulting reflectivity is in very good agreement with coincident reflectivity observed at Ku and Ka band along the full flight transect. This confirms the skills of the SSRGA to quantitatively describe the properties of ice crystals. In particular, regions of aggregates with different densities are identified: while few occurrences of active aggregation are associated with models of nearly unrimed snowflakes, the properties of ice for most of the flight correspond to slightly rimed aggregates, as it was previously found for the entire field campaign (Chase et al., 2018). This is contrasting with previous studies in very different meteorological environments (Hogan et al., 2006; Hogan et al., 2012) where it was found that ice aggregates were well described by a single mass-size relation corresponding to unrimed aggregates (Brown & Francis, 1995). Even if different models are necessary, the ice aggregates observed during OLYMPEX can

mostly be described by a much narrower range of mass-size relations (namely, those corresponding to the models SSRGA-LS15-B0.1 and SSRGA-LS15-B0.2) than what was proposed in modeling studies (Leinonen et al., 2017). At W band, a direct comparison of the reflectivity observed and modeled from the PSD is not possible because of the significant attenuation produced by the ice and liquid water present between the two aircraft.

The current work proposes a full retrieval methodology combining the observations from a suite of triple-frequency radars (Ku, Ka, and W band). Over ocean, the retrieval algorithm is also capable of assimilating the PIA obtained from the surface reference technique. For stratiform precipitation, profiles of exponential ice PSDs and gamma rain PSDs are retrieved above and below the melting layer, respectively. No retrieval is made of the melting particle properties, except for their extinction at the given radar frequencies, which is assumed to be proportional to the extinction coefficient of the rain retrieved below. This proportionality coefficient is an additional retrieved parameter for each radar frequency. As was already found by Matrosov (2008), it is close to 2.5 at Ka while it varies between [4.5;5.5] and [1;2.5] at Ku and W band, respectively.

Results confirm that the retrieval provides estimates of ice D_m and IWC which are in agreement with collocated in situ observations when a proper ice scattering model is adopted. For rain, a slightly better agreement is found when PIAs are assimilated. This confirms that, even with triple-frequency measurements, rain retrieval from reflectivity are challenging without additional observations of integrated attenuation, Doppler velocity (Mason et al., 2018) or Doppler spectra (Tridon et al., 2017). While it is not attempted to retrieve SLW, the comparison between two versions of the retrieval shows that the presence of supercooled liquid water has a limited impact on the retrieval of D_m and IWC. Since the rain and ice parts of the profiles are retrieved independently, they are used to investigate the continuity of the microphysics properties such as the mean mass diameter and the mass flux through the melting layer. For this case study, the melted mean mass diameter generally increases through the melting layer by an average of 25%, except in the regions composed of very large aggregates (i.e., with D_m as large as 8 mm) where it can decrease by as much as 20%, suggesting that large aggregates are likely to fragment into multiple droplets while melting (Leinonen & von Lerber, 2018). While the conservation of mass flux through the melting layer implies that it should not change by more than 20%, it is found that it increases by about 100% over most of the transect. Since the same behavior is found when computing the mass flux from in situ observations, it seems that this is not due to a retrieval issue but may be ascribed to a problem in the parameterization of the terminal fall velocity of raindrops and/or ice aggregates.

In summary, this intercomparison between in situ measurements and reflectivity observations and retrievals demonstrates that triple-frequency radar observations can be used to retrieve profiles of the ice and rain microphysics properties in stratiform precipitation with accuracy. In the future, these results should be confirmed with data sets including accurate direct in situ measurements of IWC. Several areas where progress is needed have been identified:

- Even with three frequencies, the retrieval of rain properties is challenging without the knowledge of integrated attenuation, and more work is needed to better understand retrieval uncertainties over land (where the PIA cannot be easily estimated).
- The availability of a limited number of ice models for different degrees of riming prevent continuous retrievals of ice properties. Future work should aim at the development and use of an ice model providing continuous description of ice properties and scattering cross sections as function of the degree of riming similarly to what was proposed by Leinonen et al. (2018) and Mason et al. (2018).
- The conservation of flux within the melting layer can be exploited to better constrain the retrieval of ice properties when rain properties are retrieved with accuracy. However, the terminal fall velocity of ice aggregates remains uncertain. Future work should aim at better assessing the range of validity of such a hypothesis.

Appendix A: Methodology Used for Ice Aggregates Classification

While it is recognized that point triple-frequency radar observations can be used to distinguish between rimed and unrimed ice particles, there is no simple method to illustrate such categorization along a profile or within a two-dimensional diagram such as the longitude-height plots of Figure 3. Therefore, a classifica-
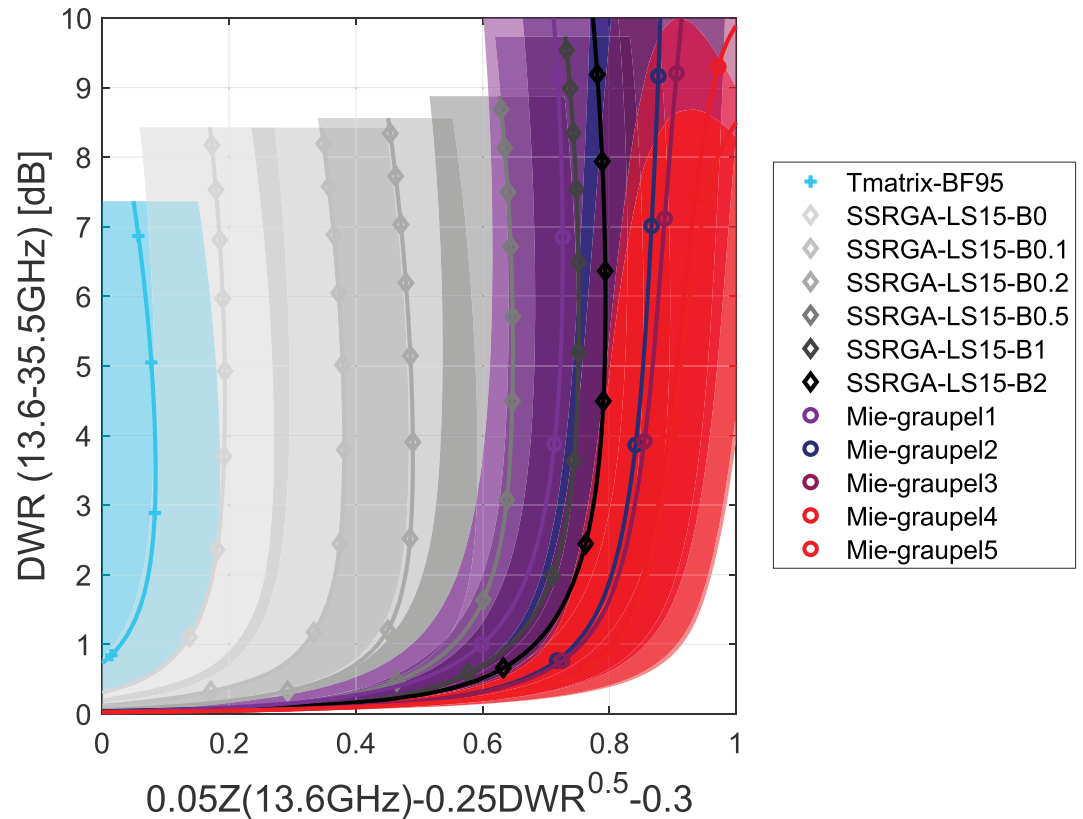
Figure A1. Variation of the riming parameter r as function of DWR_{KuKa} for most of the scattering tables described in section 3.1 and corresponding to the mass-size relations of Figure 6. The lines correspond to an IWC of 0.5 g/m^3, and shading shows the range between 0.3 and 0.8 g/m^3. DWR = dual wavelength ratio; SSRGA = Self-Similar Rayleigh-Gans Approximation.

tion of rough ice particle types (e.g., unrimed, rimed, or graupel), even approximative, is required. For weak radar signal attenuation (e.g., when there is no liquid precipitation between the target and the radar), such a method is particularly valuable because it can be applied to raw reflectivity data uncorrected for attenuation. This is found for nadir-pointing measurements, or zenith-pointing measurements with negative temperature at the ground. Furthermore, as shown in Figure 7c, the attenuation at W band is generally not negligible due to the presence of supercooled liquid water and it is therefore preferable to use lower radar frequencies such as Ku and Ka.

The combination of the absolute reflectivity at Ku band (Z_{Ku}) and the dual wavelength ratio between Ku and Ka (DWR_{KuKa}) contains information on the degree of riming of ice particles: for a fixed DWR_{KuKa}, Z_{Ku} generally increases with the degree of riming of ice particles. Furthermore, for all the scattering tables used in this study (see section 3.1), it was found that the DWR_{KuKa} practically follows a quadratic function of Z_{Ku}. The average fit of the scattering tables allows defining a riming parameter $r = 0.05 \ Z_{Ku} - 0.25 \ DWR_{KuKa}^{0.5} - 0.3$ which is practically constant for $DWR_{KuKa} > 1$ dB. Because it is normalized between 0 and 1, it looks similar to the density factor defined by Mason et al. (2018) but note that they have been defined in completely independent ways. For each scattering table, shadings in Figure A1 show the variation of r for a range of IWCs commonly found in stratiform precipitation (between 0.3 and 0.8 g/m^3). Despite some inevitable overlap between the different scattering tables, there is a clear stratification with the degree of riming of the corresponding ice particles. Because of the large uncertainty of this parameter, quantitative values are not really significant. On the other hand, one can empirically derive three qualitative ice categories: unrimed aggregates for $r < 0.33$, rimed aggregates for $0.33 < r < 0.66$ and graupel for $r > 0.66$. When DWR_{KuKa} is lower than 1 dB, the different categories cannot be easily distinguished because of the rapid increase of r, and the corresponding ice is classified as ambiguous. A final category "small ice" is defined for Z_{Ku} lower than 15 dB, where ice particles are small and DWRs always close to zero.

References

Battaglia, A., Mroz, K., Lang, T., Tridon, F., Tanelli, S., Tian, L., & Heymsfield, G. M. (2016). Using a multiwavelength suite of microwave instruments to investigate the microphysical structure of deep convective cores. *Journal of Geophysical Research: Atmospheres*, *121*, 9356–9381. https://doi.org/10.1002/2016JD025269

Battaglia, A., Mroz, K., Tanelli, S., Tridon, F., & Kirstetter, P.-E. (2016). Multiple-scattering-induced "ghost echoes" in GPM DPR observations of a tornadic supercell. *Journal of Applied Meteorology and Climatology*, *55*, 1653–1666. https://doi.org/10.1175/JAMC-D-15-0136.1

Battaglia, A., Tanelli, S., Heymsfield, G. M., & Tian, L. (2014). The dual wavelength ratio knee: A signature of multiple scattering in airborne Ku-Ka observations. *Journal of Applied Meteorology and Climatology*, *53*, 1790–1808. https://doi.org/10.1175/JAMC-D-13-0341.1

Battaglia, A., Tanelli, S., Mroz, K., & Tridon, F. (2015). Multiple scattering in observations of the GPM dual-frequency precipitation radar: Evidence and impact on retrievals. *Journal of Geophysical Research: Atmospheres*, *120*, 4090–4101. https://doi.org/10.1002/2014JD022866

Battaglia, A., Wolde, M., D'Adderio, L. P., Nguyen, C., Fois, F., Illingworth, A., & Midthassel, R. (2017). Characterization of surface radar cross sections at W-band at moderate incidence angles. *IEEE Transactions on Geoscience and Remote Sensing*, *55*(7), 3846–3859. https://doi.org/10.1109/TGRS.2017.2682423

Bennartz, R., & Petty, G. W. (2001). The sensitivity of microwave remote sensing observations of precipitation to ice particle size distributions. *Journal of Applied Meteorology*, *40*, 345–364. https://doi.org/10.1175/1520-0450(2001)040<0345:TSOMRS>2.0.CO;2

Bohren, C. F., & Huffman, D. R. (1983). *Absorption and scattering of light by small particles*. New York: John Wiley & Sons.

Botta, G., Aydin, K., Verlinde, J., Avramov, A. E., Ackerman, A. S., Fridlind, A. M., et al. (2011). Millimeter wave scattering from ice crystals and their aggregates: Comparing cloud model simulations with X- and Ka-band radar measurements. *Journal of Geophysical Research*, *116*, D00T04. https://doi.org/10.1029/2011JD015909

Brdar, S., & Seifert, A. (2018). McSnow: A Monte-Carlo particle model for riming and aggregation of ice particles in a multidimensional microphysical phase space. *Journal of Advances in Modeling Earth Systems*, *10*, 187–206. https://doi.org/10.1002/2017MS001167

Brown, P. R. A., & Francis, P. N. (1995). Improved measurements of the ice water content in cirrus using a total-water probe. *Journal of Atmospheric and Oceanic Technology*, *12*, 410. https://doi.org/10.1175/1520-0426(1995)012<0410:IMOTIW>2.0.CO;2

Chagnon, J. M., Gray, S. L., & Methven, J. (2013). Diabatic processes modifying potential vorticity in a North Atlantic cyclone. *Quarterly Journal of the Royal Meteorological Society*, *139*, 1270–1282. https://doi.org/10.1002/qj.2037

Chase, R. J., Finlon, J. A., Borque, P., McFarquhar, G. M., Nesbitt, S. W., Tanelli, S., et al. (2018). Evaluation of triple-frequency radar retrieval of snowfall properties using coincident airborne in situ observations during OLYMPEX. *Geophysical Research Letters*, *45*, 5752–5760. https://doi.org/10.1029/2018GL077997

Cober, S. G., Isaac, G. A., Korolev, A. V., & Strapp, J. W. (2001). Assessing cloud-phase conditions. *Journal of Applied Meteorology*, *40*, 1967–1983. https://doi.org/10.1175/1520-0450(2001)040<1967:ACPC>2.0.CO;2

Coronel, B., Ricard, D., Rivière, G., & Arbogast, P. (2015). Role of moist processes in the tracks of idealized midlatitude surface cyclones. *Journal of Atmospheric Sciences*, *72*, 2979–2996. https://doi.org/10.1175/JAS-D-14-0337.1

Crezee, B., Joos, H., & Wernli, H. (2017). The microphysical building blocks of low-level potential vorticity anomalies in an idealized extratropical cyclone. *Journal of Atmospheric Sciences*, *74*, 1403–1416. https://doi.org/10.1175/JAS-D-16-0260.1

D'Adderio, L. P., Porcù, F., & Tokay, A. (2018). Evolution of drop size distribution in natural rain. *Atmospheric Research*, *200*, 70–76. https://doi.org/10.1016/j.atmosres.2017.10.003

de Vries, H., Methven, J., Frame, T. H. A., & Hoskins, B. J. (2010). Baroclinic waves with parameterized effects of moisture interpreted using Rossby wave components. *Journal of Atmospheric Sciences*, *67*, 2766–2784. https://doi.org/10.1175/2010JAS3410.1

Dearden, C., Connolly, P. J., Lloyd, G., Crosier, J., Bower, K. N., Choularton, T. W., & Vaughan, G. (2014). Diabatic heating and cooling rates derived from in situ microphysics measurements: A case study of a wintertime U.K. cold front. *Monthly Weather Review*, *142*, 3100–3125. https://doi.org/10.1175/MWR-D-14-00048.1

Delanoë, J. M. E., Heymsfield, A. J., Protat, A., Bansemer, A., & Hogan, R. J. (2014). Normalized particle size distribution for remote sensing application. *Journal of Geophysical Research: Atmospheres*, *119*, 4204–4227. https://doi.org/10.1002/2013JD020700

Delanoë, J., & Hogan, R. J. (2008). A variational scheme for retrieving ice cloud properties from combined radar, lidar and infrared radiometer. *Journal of Geophysical Research*, *113*, D07204. https://doi.org/10.1029/2007JD009000

Draine, B. T., & Flatau, P. J. (1994). Discrete-dipole approximation for scattering calculations. *Journal of the Optical Society of America A*, *11*(4), 1491–1499. https://doi.org/10.1364/JOSAA.11.001491

Durden, S. L., & Tanelli, S. (2017). *GPM ground validation airborne precipitation radar 3rd generation (APR-3) OLYMPEX*. Huntsville, AL: Dataset available online from the NASA EOSDIS Global Hydrology Resource Center istributed Active Archive Center. accessed: 2017-07-20 https://doi.org/10.5067/GPMGV/OLYMPEX/APR3/DATA101

Emory, A. E., Demoz, B., Vermeesch, K., & Hicks, M. (2014). Double bright band observations with high-resolution vertically pointing radar, lidar, and profilers. *Journal of Geophysical Research: Atmospheres*, *119*, 8201–8211. https://doi.org/10.1002/2013JD020063

Erfani, E., & Mitchell, D. L. (2017). Growth of ice particle mass and projected area during riming. *Atmospheric Chemistry & Physics*, *17*, 1241–1257. https://doi.org/10.5194/acp-17-1241-2017

Fabry, F., & Zawadzki, I. (1995). Long-term radar observations of the melting layer of precipitation and their interpretation. *Journal of the Atmospheric Sciences*, *52*(7), 838–850. https://doi.org/10.1175/1520-0469(1995)052<0838:LTROOT>2.0.CO;2

Firda, J. M., Sekelsky, S. M., & McIntosh, R. E. (1999). Application of dual-frequency millimeter-wave Doppler spectra for the retrieval of drop size distributions and vertical air motion in rain. *Journal of Atmospheric and Oceanic Technology*, *16*, 216–236. https://doi.org/10.1175/1520-0426(1999)016<0216:AODFMW>2.0.CO;2

Gaussiat, N., Sauvageot, H., Illingworth, A. J., & Journal of Atmospheric and Oceanic Technology (2003). Cloud liquid water and ice content retrieval by multiwavelength radar. *Journal of Atmospheric and Oceanic Technology*, *20*, 1264–1275. https://doi.org/10.1175/1520-0426(2003)020<1264:CLWAIC>2.0.CO;2

Grams, C. M., Wernli, H., Böttcher, M., Čampa, J., Corsmeier, U., Jones, S. C., et al. (2011). The key role of diabatic processes in modifying the upper-tropospheric wave guide: A North Atlantic case-study. *Quarterly Journal of the Royal Meteorological Society*, *137*, 2174–2193. https://doi.org/10.1002/qj.891

Grecu, M., Olson, W. S., Munchak, S. J., Ringerud, S., Liao, L., Haddad, Z., et al. (2016). The GPM combined algorithm. *Journal of Atmospheric and Oceanic Technology*, *33*, 2225–2245. https://doi.org/10.1175/2011JAMC2655.1

Grecu, M., Tian, L., Olson, W. S., & Tanelli, S. (2011). A robust dual-frequency radar profiling algorithm. *Journal of Atmospheric and Oceanic Technology*, *50*, 1543–1557. https://doi.org/10.1175/JTECH-D-16-0019.1

Hartmann, D. L., Hendon, H. H., & Houze, R. A. (1984). Some implications of the mesoscale circulations in tropical cloud clusters for large-scale dynamics and climate. *Journal of Atmospheric Sciences*, *41*, 113–121. https://doi.org/10.1175/1520-0469(1984)041<0113: SIOTMC>2.0.CO;2

Heymsfield, A. J. (1982). A comparative study of the rates of development of potential graupel and hail embryos in high plains storms. *Journal of the Atmospheric Sciences*, *39*, 2867–2897. https://doi.org/10.1175/1520-0469(1982)039<2867:ACSOTR>2.0.CO;2

Heymsfield, A., Bansemer, A., & Poellot, M. (2017). *GPM Ground Validation NCAR particle probes OLYMPEX*. Huntsville, AL: Dataset available online from the NASA EOSDIS Global Hydrology Resource Center Distributed Active Archive Center. Accessed: 2017-07-20.

Heymsfield, A. J., Bansemer, A., Schmitt, C., Twohy, C., & Poellot, M. R. (2004). Effective ice particle densities derived from aircraft data. *Journal of the Atmospheric Sciences*, *61*, 982–1003. https://doi.org/10.1175/1520-0469(2004)061<0982:EIPDDF>2.0.CO;2

Heymsfield, A., Bansemer, A., Wood, N. B., Liu, G., Tanelli, S., Sy, O. O., et al. (2018). Toward improving ice water content and snow-rate retrievals from radars. Part II: Results from three wavelength radar-collocated in-situ measurements and CloudSat-GPM-TRMM radar data. *Journal of Applied Meteorology and Climatology*, *57*, 365–389. https://doi.org/10.1175/JAMC-D-17-0164.1

Heymsfield, A. J., & Westbrook, C. D. (2010). Advances in the estimation of ice particle fall speeds using laboratory and field measurements. *Journal of the Atmospheric Sciences*, *67*, 2469–2482. https://doi.org/10.1175/2010JAS3379.1

Hogan, R. J., & Battaglia, A. (2008). Fast lidar and radar multiple-scattering models: Part 2: Wide-angle scattering using the time-dependent two-stream approximation. *Journal of the Atmospheric Sciences*, *65*, 3636–3651. https://doi.org/10.1175/2008JAS2643.1

Hogan, R. J., Honeyager, R., Tyynelä, J., & Kneifel, S. (2017). Calculating the millimetre-wave scattering phase function of snowflakes using the self-similar Rayleigh-Gans approximation. *Quarterly Journal of the Royal Meteorological Society*, *143*, 834–844. https://doi.org/10.1002/qj.2968

Hogan, R. J., Mittermaier, M. P., & Illingworth, A. J. (2006). The retrieval of ice water content from radar reflectivity factor and temperature and its use in evaluating a mesoscale model. *Journal of Applied Meteorology and Climatology*, *45*, 301–317. https://doi.org/10.1175/JAM2340.1

Hogan, R. J., Tian, L., Brown, P. R. A., Westbrook, C. D., Heymsfield, A. J., & Eastment, J. D. (2012). Radar scattering from ice aggregates using the horizontally aligned oblate spheroid approximation. *Journal of Applied Meteorology and Climatology*, *51*, 655–671. https://doi.org/10.1175/JAMC-D-11-074.1

Hogan, R. J., & Westbrook, C. D. (2014). Equation for the microwave backscatter cross section of aggregate snowflakes using the self-similar Rayleigh-Gans approximation. *Journal of Atmospheric Sciences*, *71*, 3292–3301. https://doi.org/10.1175/JAS-D-13-0347.1

Houze, R. A. (1982). Cloud clusters and large-scale vertical motions in the tropics. *Journal of the Meteorological Society of Japan*, *60*, 396–410. https://doi.org/10.2151/jmsj1965.60.1_396

Houze, R. A. (1989). Observed structure of mesoscale convective systems and implications for large-scale heating. *Quarterly Journal of the Royal Meteorological Society*, *115*, 425–461. https://doi.org/10.1002/qj.49711548702

Houze, R. A., McMurdie, L. A., Petersen, W. A., Schwaller, M. R., Baccus, W., Lundquist, J. D., et al. (2017). The Olympic Mountains experiment (OLYMPEX). *Bulletin of the American Meteorological Society*, *98*, 2167–2188. https://doi.org/10.1175/BAMS-D-16-0182.1

Jackson, R. C., McFarquhar, G. M., Stith, J., Beals, M., Shaw, R. A., Jensen, J., et al. (2014). An assessment of the impact of antishattering tips and artifact removal techniques on cloud ice size distributions measured by the 2D cloud probe. *Journal of Atmospheric and Oceanic Technology*, *31*, 2567–2590. https://doi.org/10.1175/JTECH-D-13-00239.1

Joos, H., & Wernli, H. (2012). Influence of microphysical processes on the potential vorticity development in a warm conveyor belt: A case-study with the limited-area model OSMO. *Quarterly Journal of the Royal Meteorological Society*, *138*, 407–418. https://doi.org/10.1002/qj.934

Kneifel, S., Kollias, P., Battaglia, A., Leinonen, J., Maahn, M., Kalesse, H., & Tridon, F. (2016). First observations of triple-frequency radar Doppler spectra in snowfall: Interpretation and applications. *Geophysical Research Letters*, *43*, 2225–2233. https://doi.org/10.1002/2015GL067618

Kneifel, S., von Lerber, A., Tiira, J., Moisseev, D., Kollias, P., & Leinonen, J. (2015). Observed relations between snowfall microphysics and triple-frequency radar measurements. *Journal of Geophysical Research: Atmospheres*, *120*, 6034–6055. https://doi.org/10.1002/2015JD023156

Kollias, P., & Albrecht, B. (2005). Why the melting layer radar reflectivity is not bright at 94 Hz. *Geophysical Research Letters*, *32*, L24818. https://doi.org/10.1029/2005GL024074

Korolev, A., Strapp, J. W., Isaac, G. A., & Emery, E. (2013). Improved airborne hot-wire measurements of ice water content in clouds. *Journal of Atmospheric and Oceanic Technology*, *30*, 2121–2131. https://doi.org/10.1175/JTECH-D-13-00007.1

L'Ecuyer, T. S., & Stephens, G. L. (2002). An estimation-based precipitation retrieval algorithm for attenuating radars. *Journal of Applied Meteorology*, *41*, 272–285. https://doi.org/10.1175/1520-0450(2002)041<0272:AEBPRA>2.0.CO;2

Lawson, R. P., O'Connor, D., Zmarzly, P., Weaver, K., Baker, B., Mo, Q., & Jonsson, H. (2006). The 2D-S (Stereo) probe: Design and preliminary tests of a new airborne, high-speed, high-resolution particle imaging probe. *Journal of Atmospheric and Oceanic Technology*, *23*, 1462. https://doi.org/10.1175/JTECH1927.1

Leinonen, J. (2014). High-level interface to T-matrix scattering calculations: architecture, capabilities and limitations. *Optics Express*, *22*, 1655. https://doi.org/10.1364/OE.22.001655

Leinonen, J., Kneifel, S., & Hogan, R. J. (2017). Evaluation of the Rayleigh-Gans approximation for microwave scattering by rimed snowflakes. *Quarterly Journal of the Royal Meteorological Society*, *144*, 77–88. https://doi.org/10.1002/qj.3093

Leinonen, J., Lebsock, M. D., Tanelli, S., Sy, O. O., Dolan, B., Chase, R. J., et al. (2018). Retrieval of snowflake microphysical properties from multi-frequency radar observations. *Atmospheric Measurement Techniques*, *11*, 5471–5488. https://doi.org/10.1002/2017JD027909

Leinonen, J., Moisseev, D., & Nousiainen, T. (2013). Linking snowflake microstructure to multi-frequency radar observations. *Journal of Geophysical Research: Atmospheres*, *118*, 3259–3270. https://doi.org/10.1002/jgrd.50163

Leinonen, J., & Szyrmer, W. (2015). Radar signatures of snowflake riming: A modeling study. *Earth and Space Science*, *2*, 346–358. https://doi.org/10.1002/2015EA000102

Leinonen, J., & von Lerber, A. (2018). Snowflake melting simulation using smoothed particle hydrodynamics. *Journal of Geophysical Research: Atmospheres*, *123*(3), 1811–1825. https://doi.org/10.1002/2017JD027909

Lhermitte, R. (1990). Attenuation and scattering of millimeter wavelength radiation by clouds and precipitation. *Journal of Atmospheric and Oceanic Technology*, *7*, 464–479. https://doi.org/10.1175/1520-0426(1990)007<0464:AASOMW>2.0.CO;2

Li, H., Moisseev, D., & von Lerber, A. (2018). How does riming affect dual-polarization radar observations and snowflake shape? *Journal of Geophysical Research: Atmospheres*, *123*, 6070–6081. https://doi.org/10.1029/2017JD028186

Liebe, H. J. (1989). MPM—An atmospheric millimeter-wave propagation model. *International Journal of Infrared and Millimeter Waves*, *10*, 631–650. https://doi.org/10.1007/BF01009565

Liu, C., Shige, S., Takayabu, Y. N., & Zipser, E. (2015). Latent heating contribution from precipitation systems with different sizes, depths, and intensities in the tropics. *Journal of Climate*, *28*, 186–203. https://doi.org/10.1175/JCLI-D-14-00370.1

Mace, G. G., Avey, S., Cooper, S., Lebsock, M., Tanelli, S., & Dobrowalski, G. (2016). Retrieving co-occurring cloud and precipitation properties of warm marine boundary layer clouds with A-Train data. *Journal of Geophysical Research: Atmospheres*, *121*, 4008–4033. https://doi.org/10.1002/2015JD023681

Marinescu, P. J., van den Heever, S. C., Saleeby, S. M., & Kreidenweis, S. M. (2016). The microphysical contributions to and evolution of latent heating profiles in two MC3E MCSs. *Journal of Geophysical Research: Atmospheres*, *121*, 7913–7935. https://doi.org/10.1002/2016JD024762

Mason, S. L., Chiu, C. J., Hogan, R. J., Moissev, D., & Kneifel, S. (2018). Retrievals of riming and snow particle density from vertically-pointing Doppler radars. *Journal of Geophysical Research: Atmospheres*, *123*. https://doi.org/10.1029/2018JD028603

Mason, S. L., Chiu, J. C., Hogan, R. J., & Tian, L. (2017). Improved rain rate and drop size retrievals from airborne Doppler radar. *Atmospheric Chemistry and Physics*, *17*, 11,567–11,589. https://doi.org/10.5194/acp-17-11567-2017

Mason, S. L., Hogan, R. J., Westbrook, C. D., Kneifel, S., & Moisseev, D. (2019). The importance of particle size distribution shape for triple-frequency radar retrievals of the morphology of snow. *Atmospheric Measurement Techniques Discussions*, 1–30. https://doi.org/10.5194/amt-2019-100

Matrosov, S. Y. (1998). A dual-wavelength radar method to measure snowfall rate. *Journal of Applied Meteorology*, *37*, 1510–1521. https://doi.org/10.1175/1520-0450(1998)037<1510:ADWRMT>2.0.CO;2

Matrosov, S. Y. (2008). Assessment of radar signal attenuation caused by the melting hydrometeor layer. *IEEE Transactions on Geoscience and Remote Sensing*, *46*(4), 1039–1047. https://doi.org/10.1109/TGRS.2008.915757

Mätzler, C., Ellison, W., Thomas, B., Sihvola, A., & Schwank, M. (2005). Thermal microwave radiation: Applications for remote sensing. Christian Mätzler.

Meneghini, R., Liao, L., Tanelli, S., & Durden, S. L. (2012). Assessment of the performance of a dual-frequency surface reference technique over ocean. *IEEE Transactions on Geoscience and Remote Sensing*, *50*, 2968–2977. https://doi.org/10.1109/TGRS.2011.2180727

Mie, G. (1908). Beiträge zur Optik trüber Medien, speziell kolloidaler Metallösungen. *Annalen der Physik*, *330*, 377–445. https://doi.org/10.1002/andp.19083300302

Mishchenko, M. I. (2000). Calculation of the amplitude matrix for a nonspherical particle in a fixed orientation. *Applied Optics*, *39*, 1026–1031. https://doi.org/10.1364/AO.39.001026

Mishchenko, M. I., Travis, L. D., & Mackowski, D. W. (1996). T-matrix computations of light scattering by nonspherical particles: A review. *Journal of Quantitative Spectroscopy and Radiation Transfer*, *55*, 535–575. https://doi.org/10.1016/0022-4073(96)00002-7

Moisseev, D., von Lerber, A., & Tiira, J. (2017). Quantifying the effect of riming on snowfall using ground-based observations. *Journal of Geophysical Research: Atmospheres*, *122*, 4019–4037. https://doi.org/10.1002/2016JD026272

Morrison, H., & Milbrandt, J. A. (2015). Parameterization of cloud microphysics based on the prediction of bulk ice particle properties. Part i: Scheme description and idealized tests. *Journal of the Atmospheric Sciences*, *72*(1), 287–311. https://doi.org/10.1175/JAS-D-14-0065.1

Munchak, S. J., & Kummerow, C. D. (2011). A modular optimal estimation method for combined radar-radiometer precipitation profiling. *Journal of Applied Meteorology and Climatology*, *50*, 433–448. https://doi.org/10.1175/2010JAMC2535.1

Ori, D., Maestri, T., Rizzi, R., Cimini, D., Montopoli, M., & Marzano, F. S. (2014). Scattering properties of modeled complex snowflakes and mixed-phase particles at microwave and millimeter frequencies. *Journal of Geophysical Research: Atmospheres*, *119*, 9931–9947. https://doi.org/10.1002/2014JD021616

Papritz, L., & Spengler, T. (2015). Analysis of the slope of isentropic surfaces and its tendencies over the North Atlantic. *Quarterly Journal of the Royal Meteorological Society*, *141*, 3226–3238. https://doi.org/10.1002/qj.2605

Petersen, Z., & Houze, R. A. (2017). *GPM ground validation campaign reports OLYMPEX*. Huntsville, AL: Dataset available online from the NASA EOSDIS Global Hydrology Resource Center Distributed Archive Center. Accessed: 2017-07-20.

Petty, G. W., & Huang, W. (2010). Microwave backscatter and extinction by soft ice spheres and complex snow aggregates. *Journal of Atmospheric Sciences*, *67*, 769–787. https://doi.org/10.1175/2009JAS3146.1

Poellot, M., Heymsfield, A., & Bansemer, A. (2017). *GPM ground validation UND citation cloud microphysics OLYMPEX*. Huntsville, AL: Dataset available online from the NASA EOSDIS Global Hydrology Resource Center Distributed Active Archive Center. Accessed: 2017-07-20.

Protat, A., Delanoë, J., Bouniol, D., Heymsfield, A. J., Bansemer, A., & Brown, P. (2007). Evaluation of ice water content retrievals from cloud radar reflectivity and temperature using a large airborne in situ microphysical database. *Journal of Atmospheric and Oceanic Technology*, *46*, 557–572. https://doi.org/10.1175/JAM2488.1

Ray, P. S. (1972). Broadband complex refractive indices of ice and water. *Applied Optics*, *11*, 1836. https://doi.org/10.1364/AO.11.001836

Rodgers, C. D. (2000). *Inverse methods for atmospheric sounding: Theory and practice*. River Edge, NJ: World Scientific. 238 pp.

Rosenkranz, P. W. (1993). Absorption of microwaves by atmospheric gases. In M. A. Janssen (Ed.), *Atmospheric remote sensing by microwave radiometry*, pp. (37–79) New York: Wiley.

Rosenkranz, P. W. (1998). Water vapor microwave continuum absorption: A comparison of measurements and models. *Radio Science*, *33*(4), 919–928. https://doi.org/10.1029/98RS01182

Sadowy, G. A., Berkun, A. C., Chun, W., Im, E., & Durden, S. L. (2003). Development of an advanced airborne precipitation radar. *Microwave Journal*, *46*(1), 84–98.

Schumacher, C., Houze, R. A., & Kraucunas, I. (2004). The tropical dynamical response to latent heating estimates derived from the TRMM precipitation radar. *Journal of Atmospheric Sciences*, *61*, 1341–1358. https://doi.org/10.1175/1520-0469(2004)061<1341:TTDRTL>2.0.CO;2

Seifert, A., Leinonen, J., Siewert, C., & Kneifel, S. (2019). The geometry of rimed aggregate snowflakes: A modeling study. *Journal of Advances in Modeling Earth Systems*, *11*, 712–731. https://doi.org/10.1029/2018MS001519

Seto, S., Iguchi, T., & Oki, T. (2013). The basic performance of a precipitation retrieval algorithm for the global precipitation measurement mission's single/dual-frequency radar measurements. *IEEE Transactions on Geoscience and Remote Sensing*, *51*, 5239–5251. https://doi.org/10.1109/TGRS.2012.2231686

Stein, T. H. M., Westbrook, C. D., & Nicol, J. C. (2015). Fractal geometry of aggregate snowflakes revealed by triple-wavelength radar measurements. *Geophysical Research Letters*, *42*, 176–183. https://doi.org/10.1002/2014GL062

Tanelli, S., Durden, S. L., & Im, E. (2006). Simultaneous measurements of Ku- and Ka-band sea surface cross sections by an airborne radar. *IEEE Geoscience and Remote Sensing Letters*, *3*, 359–363. https://doi.org/10.1109/LGRS.2006.872929

Tao, W.-K., Iguchi, T., & Lang, S. (2019). Improved Goddard latent heating algorithm for GPM extra-tropical retrievals based on NU-WRF simulation. *Journal of Applied Meteorology and Climatology*, *58*, 921–946. https://doi.org/10.1175/JAMC-D-18-0215.1

Testud, J., Oury, S., Black, R. A., Amayenc, P., & Dou, X. (2001). The concept of 'normalized' distribution to describe raindrop spectra: A tool for cloud physics and cloud remote sensing. *Journal of Applied Meteorology*, *40*, 1118–1140. https://doi.org/10.1175/1520-0450(2001)040<1118:TCONDT>2.0.CO;2

Tridon, F., & Battaglia (2015). Dual-frequency radar Doppler spectral retrieval of rain drop size distributions and entangled dynamics variables. *Journal of Geophysical Research: Atmospheres*, *120*, 5585–5601. https://doi.org/10.1002/2014JD023023

Tridon, F., Battaglia, A., & Kollias, P. (2013). Disentangling Mie and attenuation effects in rain using a K_a-W dual-wavelength Doppler spectral ratio technique. *Geophysical Research Letters*, *40*, 5548–5552. https://doi.org/10.1002/2013GL057454

Tridon, F., Battaglia, A., Luke, E., & Kollias, P. (2017). Rain retrieval from dual-frequency radar Doppler spectra: Validation and potential for a midlatitude precipitating case-study. *Quarterly Journal of the Royal Meteorological Society*, *143*, 1364–1380. https://doi.org/10.1002/qj.3010

Turk, F. J., Park, K.-W., Haddad, Z. S., Rodriguez, P., & Hudak, D. R. (2011). Constraining CloudSat-based snowfall profiles using surface observations and c-band ground radar. *Journal of Geophysical Research*, *116*. https://doi.org/10.1029/2011JD016126

Tyynelä, J., Leinonen, J., Moisseev, D., & Nousiainen, T. (2011). Radar backscattering from snowflakes: Comparison of fractal, aggregate, and soft spheroid models. *Journal of Atmospheric and Oceanic Technology*, *28*, 1365–1372. https://doi.org/10.1175/JTECH-D-11-00004.1

Tyynelä, J., Leinonen, J., Westbrook, C. D., Moisseev, D., & Nousiainen, T. (2013). Applicability of the Rayleigh-Gans approximation for scattering by snowflakes at microwave frequencies in vertical incidence. *Journal of Geophysical Research: Atmospheres*, *118*, 1826–1839. https://doi.org/10.1002/jgrd.50167

Williams, C. R., Bringi, V. N., Carey, L. D., Chandrasekar, V., Gatlin, P. N., Haddad, Z. S., et al. (2014). Describing the shape of raindrop size distributions using uncorrelated raindrop mass spectrum parameters. *Journal of Applied Meteorology and Climatology*, *53*, 1282–1296. https://doi.org/10.1175/JAMC-D-13-076.1

Willison, J., Robinson, W. A., & Lackmann, G. M. (2013). The importance of resolving mesoscale latent heating in the North Atlantic storm track. *Journal of Atmospheric Sciences*, *70*, 2234–2250. https://doi.org/10.1175/JAS-D-12-0226.1

Yin, M., Liu, G., Honeyager, R., & Joseph Turk, F. (2017). Observed differences of triple-frequency radar signatures between snowflakes in stratiform and convective clouds. *Journal of Quantitative Spectroscopy and Radiative Transfer*, *193*, 13–20. https://doi.org/10.1016/j.jqsrt.2017.02.017